DEVELOPMENT OF RADAR ALTIMETRY DATA PROCESSING IN THE OCEANIC COASTAL ZONE

ESA/ESRIN Contract No. 21201/08/I-LG (CCN 3)

Deliverable on

Data combination and GPD validation

Version 1.1

Code	COASTALT-D2.1d-1.1	**Edition**	1.1	**Date**	29-09-2011
Client	European Space Agency	**Final User**		-	

	Name	Signature	Date
Written by	UPorto (Joana Fernandes, Clara Lázaro, Alexandra Nunes)		29/09/2011
Approved by			
Revised by			
Authorised by			

DISSEMINATION	COPIES	MEANS
ESA, Jérôme Benveniste, Salvatore Dinardo and Bruno Lucas	1	Electronic
NOC, Paolo Cipollini	1	Electronic

SUMMARY OF MODIFICATIONS

Ed.	Date	Chapter	Modification	Author/s
1.1	29/09/2011	1.2.1	Definition of the variable Nr on equation 3	J. Fernandes
1.1	29/09/2011	1.2.1	Equation 3 was rewritten	J. Fernandes
1.1	29/09/2011	1.2.1	On page 11, the mean values of the Gaussian scale factor and the correlation scale of the example grid were corrected (they were swapped)	J. Fernandes
1.1	29/09/2011	1.2.1	The legend of Figure 9 was corrected	J. Fernandes
1.1	29/09/2011	1.2.1	Figures 12 and 13 were inserted. Explanatory text was inserted before figure 10.	J. Fernandes
1.1	29/09/2011	2.6	Figures 34 to 48 were inserted. Explanatory text was added before Table 1 and after Figure 52	J. Fernandes

TABLE OF CONTENTS

Reference Documents

[RD1] **COASTALT Project Management Plan v1.3,** COASTALT2-PMP-13, February 7, 2011

[RD2] **Wet Tropospheric Corrections in Coastal Areas**, COASTALT Deliverable D2.1b v1.2, 30/06/2009

[RD3] **Global assessment of GNSS-derived tropospheric corrections**, COASTALT CCN3 Deliverable D2.1a v1.1, 26/07/2010

[RD4] **GPD Global implementation**, COASTALT CCN3 Deliverable D2.1c v1.0, 15/04/2011

Acronyms

2T - 2-meter Temperature
AMR – Advanced Microwave Radiometer
ECMWF - European Centre for Medium-Range Weather Forecasts
ESA – European Space Agency
GDR – Geophysical Data Record
GNSS - Global Navigation Satellite System
GPD - GNSS-derived Path Delay
JMR – Jason Microwave Radiometer
JPL – Jet Propulsion Laboratory
LPA – Land Proportion Algorithm
MPA – Mixed-Pixel Algorithm
MWR - MicroWave Radiometer
PD – Path Delay
PISTACH – Prototype Innovant de Système de Traitement pour les Applications Côtières et Hydrologiques
RADS - Radar Altimeter Database System
RD1 – Reference Document 1
RD2 – Reference Document 2
RD3 – Reference Document 3
RD4 – Reference Document 4
SLP - Sea Level Pressure
SSM/I - Special Sensor Microwave Imager
SurfP- Surface pressure
T_B – Brightness Temperature
TCWV - Total Column Water Vapour
TMR – TOPEX Microwave Radiometer
UPorto - University of Porto
ZWD – Zenith Wet Delay

Introduction

This document presents the Deliverable D2.1d for the COASTALT project, CCN 3, CONTRACT No. 20698/07/I-LG and is delivered for fulfilment of milestone M12.

The present report describes the work that has been done at University of Porto (UPorto) concerning the spatial correlation scales of the Zenith Wet Delay (ZWD) field and the GNSS-derived path delay (GPD) validation.

The document is divided in 3 sections. Section 1 presents the work related with the determination of the spatial correlation scales of the ZWD field. Section 2 presents the GPD validation at global scale. The main conclusions are summarized in section 3.

1 Spatial Correlation function of the ZWD field

1.1 Objective analysis

At a given location along the ground satellite track with invalid Microwave Radiometer (MWR) correction, the GPD algorithm estimates the wet tropospheric correction, or ZWD, from a combination of the available data types within the specified spatial and temporal influence regions.

The data types used are the valid MWR measurements, Global Navigation Satellite System (GNSS) derived path delay at a network of coastal stations and ZWD computed from the European Centre for Medium-Range Weather Forecasts (ECMWF). Details about the pre-processing required for each data type have been given in previous reports, namely on [RD4]

The details about the GPD implementation were presented in [RD2] and are reviewed here.

The statistical technique interpolates the wet tropospheric correction at the latter locations and epochs from nearby (in time and space) independent measurements and provides the quantification of the interpolation errors by taking into account the respective accuracy of each data set.

The technique also requires *a priori* information regarding the statistics of signal and noise variability and, given these parameters, estimates are optimal in the sense that no more accurate linear combinations of the observations, based on a least squares criterion, exist (Bretherton et al. 1976). Spatial covariances between each pair of observations and each observation and the location at which an estimate is required can be derived from a Gauss-Markov function (Schüler 2001), providing that the spatial correlation scale is known. To take into account the time variability of the ZWD field, an interpolation in time is also required and, therefore, the space-time correlation function shall be obtained by multiplying the space correlation function by a stationary Gaussian decay.

Bosser et al. (2007) refer that the ZWD varies spatially and temporally with typical scales of 1 to 100 km and 1 to 100 minutes, respectively, and these ranges allow a preliminary establishment of the spatial and temporal correlation scales.

In Fernandes et al. (2010) the following correlation functions were adopted: In the absence of the knowledge of an empirical covariance model of the background field, a covariance function $F(r)$ that decreases exponentially with the square of the distance between acquisitions was adopted:

$$F(r) = e^{-\frac{r^2}{C^2}} \qquad (1)$$

where r is the distance between each pair of points and C is the spatial correlation scale The spatial correlation scale assumes that the field is isotropic and has been set to 100 km (Bosser et al. 2007).

The temporal variability of the field is also taken into account and the covariance function is represented by a space-time analytical function $G(r,\Delta t)$

that is obtained by multiplying the space correlation function $F(r)$ by a stationary Gaussian decay of the form:

$$D(\Delta t) = e^{-\frac{\Delta t^2}{T^2}} \quad (2)$$

where Δt is the time interval between the acquisition of the measurements associated to each pair of locations and T is the temporal correlation scale, set to 100 minutes (Bosser et al. 2007). Both the temporal and spatial correlation scales were assumed to remain constant over the study region.

MWR- and GNSS-derived observations were assumed to have the same white measurement noise of 5 mm, while a value of 1 cm was assigned to white noise of the model-derived estimates.

More accurate estimates of the correlation scales can be obtained by the fitting of the empirical autocorrelation function. This section presents the work that has been performed in order to improve the described data combination methodology by attempting an improved estimation of the empirical spatial auto-correlation function. The temporal correlation function will not be addressed here and will be subject of future work.

1.2 Estimation of the spatial correlation function

1.2.1 Determination of spatial correlation scale assuming isotropy

The procedure adopted here assumes that the autocorrelation of the ZWD field is isotropic, that is, the covariance and correlation between two points, x_i and x_j, are function of their distance r only, and not of their specific locations.

The analysis is performed on ECMWF global grids, with a spatial sampling of 0.25° both in latitude and longitude and a temporal sampling of 6 hours;

Each analysis is performed on a single grid, for a given epoch. This way, only the spatial variability is analysed. Then, the analysis is repeated for various grids at different epochs to evaluate how the results vary with time.

For each ZWD grid, the space domain is divided into regions of equal size in latitude and longitude, for example squares of 5 degrees width. These regions have to be large enough to include the main spatial scales of variability of the ZWD field and small enough to evaluate how the autocorrelation function varies from one region to another.

For simplicity, let's call each of these regions A, for example a square of 5° width. The procedure implemented to perform the analysis of the correlation scales in each region A is explained next.

1) Let N be the set of points on region A. These points can form $M=N\,(N-1)/2$ different pairs of points. For each pair the distance between

the points (x_i, x_i) can be computed and the points grouped in classes of distances with a fixed interval Δr of, for example, 10 km.

2) Let r be a given class of distances, for example $r_i \leq r \leq r_i + \Delta r$, where Δr is for example 10 km. For each distance class r, the semi-variogram of the points belonging to this class is given by

$$\gamma(r) = \frac{1}{2N_r}\sum_{k=1}^{N_r}\left(x_i - x_j\right)^2 \quad (3)$$

where $\left(x_i, x_j\right)$ are the points belonging to set S_r, that is the set of points for which the distance between them is $r_i \leq r \leq r_i$ and N_r is the number of points belonging to set S_r.

3) The covariance of the points on set S_r is given by:
$\mathrm{Cov}(r) = \sigma_r^2 - \gamma(r)$ (4)

4) The correlation of the points on set S_r is given by:
$\mathrm{Cor}(r) = \frac{\sigma_r^2 - \gamma(r)}{\sigma_r^2} = 1 - \frac{\gamma(r)}{\sigma_r^2}$ (5)
where σ_r^2 is the variance of set S_r

5) Repeating this procedure for all classes of distances up to a maximum distance $\mathrm{d_{max}}$ of, for example, 500 km, we end up with tables $(r_i, \gamma(r_i),)$ and $(r_i, cor(r_i),)$ of the empirical semi-variogram and autocorrelation, respectively. The autocorrelation function of the analysed field will be a function which fits in some sense the empirical autocorrelation table.

6) For each spatial cell a Gaussian function of the form (1) is adjusted to the correlation's table by least squares fitting and the scale factor C is determined. In addition, the distance D for which the correlation is zero is also computed by linear interpolation from the correlation table values.

The distances used in these computations are the spherical distances between the points. The distance associated to each class is the mean distance for all the N_r pairs of points.

This procedure was applied to various ECMWF grids, using different sizes for the cells where each analysis is performed.

Figure 1 represents the mean ZWD field for the period 2008-2009 computed from all ECMWF grids for this period. Figure 2 presents the ZWD field for the ECMWF grid at 0h on 01/01/2009, from now on called grid_ 2009_ZWD_Full. Figure 3 shows the residual or anomalous ZWD field for the same epoch (0h on 01/01/2009) obtained by subtracting the mean field to the total ZWD values. This grid will be called grid_2009_ZWD_Res.

Figures 4 to 6 show the scale factor C of the adjusted Gaussian for ECMWF grid_2009_ZWD_Full using cells of size 2.5°x2.5°, 5°x5° and 10°x10°

respectively. The results for the residual grid grid_2009_ZWD_Res (not shown here) are very similar to those obtained for the full field.

Figures 7 and 8 illustrate the results, now for the distance D for which the correlation becomes zero, here designated by correlation scale, for grid_2009_ZWD_Full using cells of size 2.5°x2.5° and 5°x5° respectively.

The results show that both the Gaussian scale factor C and the correlation scale D increase with the size of the analysed cells, being minimum for the 2.5°x2.5° and maximum for the 10°x10° cells. This happens both for the full and the residual fields.

In section 1.3 we show the results of a study aiming to investigate ways to remove the dependency of the result on the size of the analysed domain. Here we just summarize the results obtained with the full and residual ZWD fields.

We already mentioned the large and puzzling dependence of the analysed scales on the size of the domain. In summary, for the correlation scale, the mean values for grid_2009_ZWD_Full are: 118, 210 and 380 km for grids of size 2.5°x2.5°, 5°x5° and 10°x10°, respectively. The corresponding values for the Gaussian scale factor are: 88, 154 and 276 km.

For the anomalous ZWD grid (grid_2009_ZWD_Res) the mean values are very similar to those obtained for the mean field, with differences of the order of 1 to 3 km.

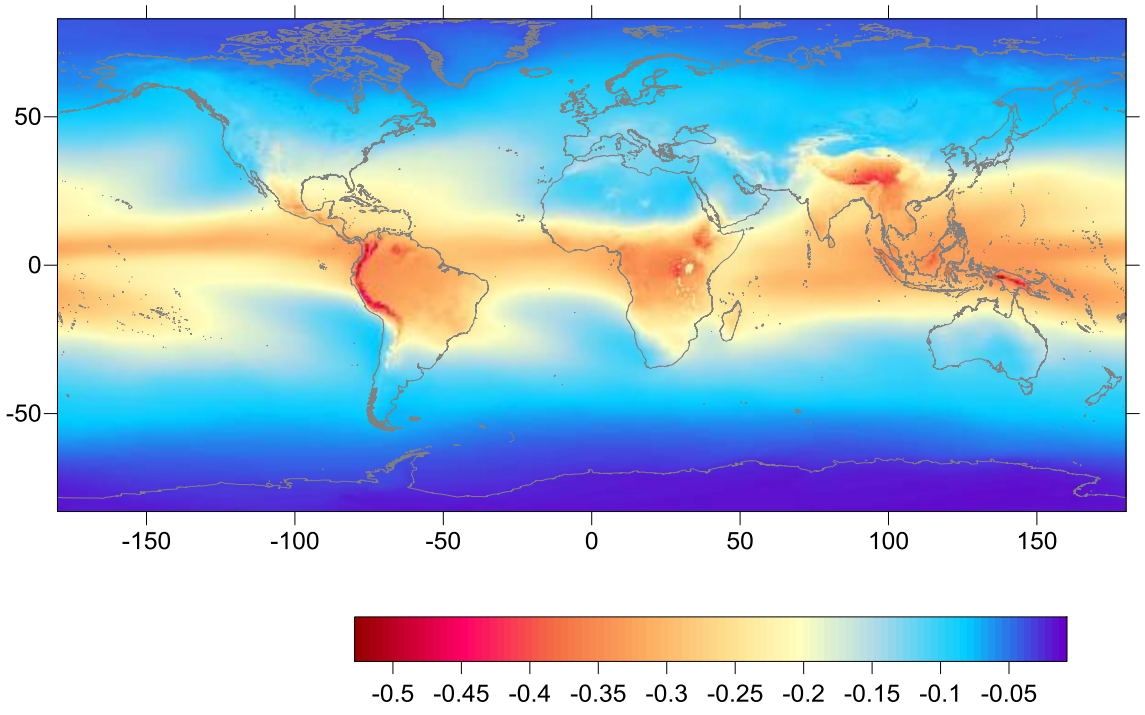

Fig.1 – Mean ZWD field of ECMWF for the period 2008-2009, in metres.

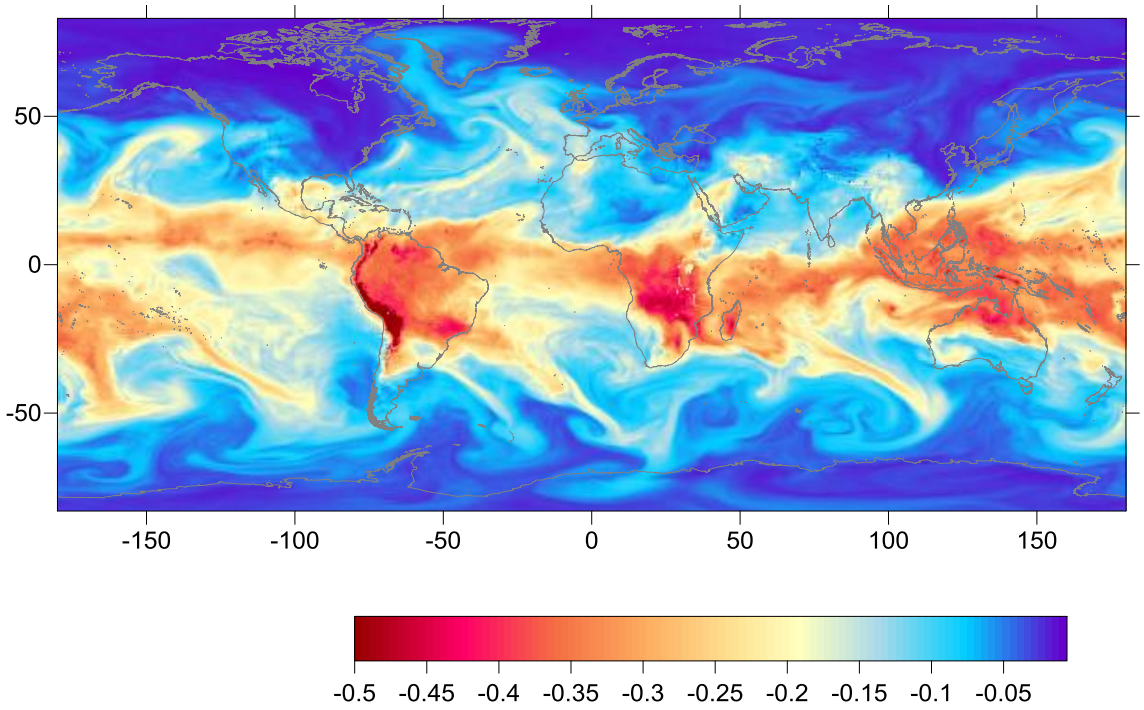

Fig.2 – ZWD field of ECMWF grid on 0h of 01/01/2009, in metres (grid_2009_ZWD_Full).

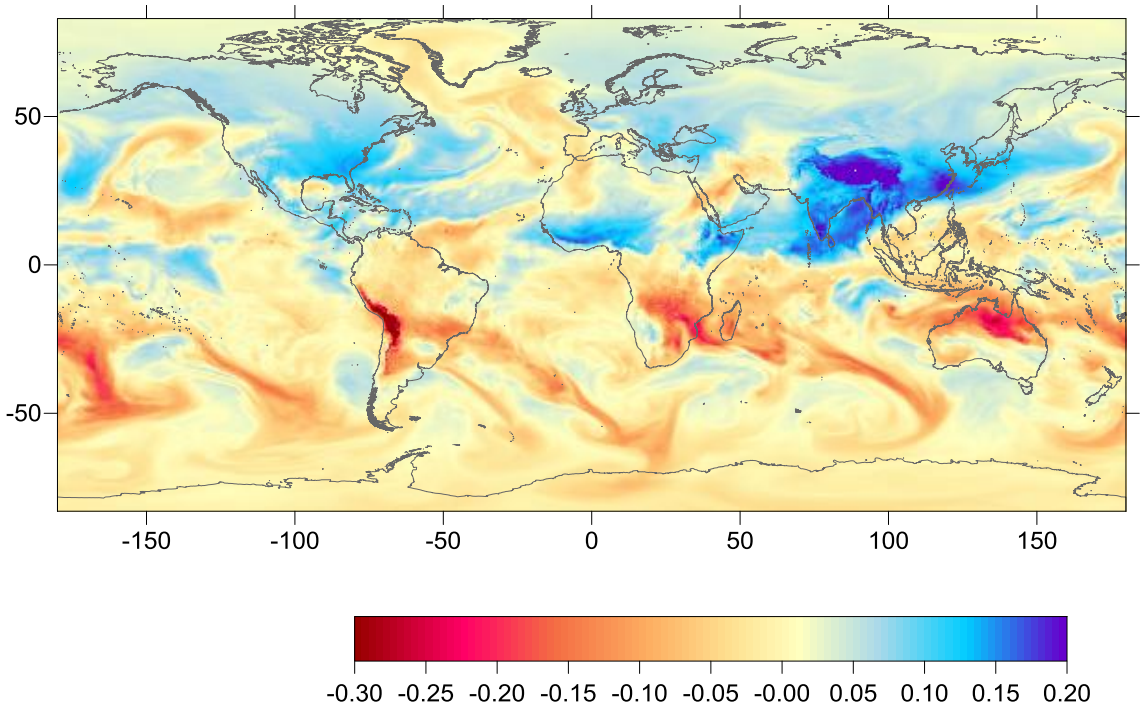

Fig. 3 – Residual ZWD field of ECMWF grid on 0h of 01/01/2009, in metres (grid_2009_ZWD_Res).

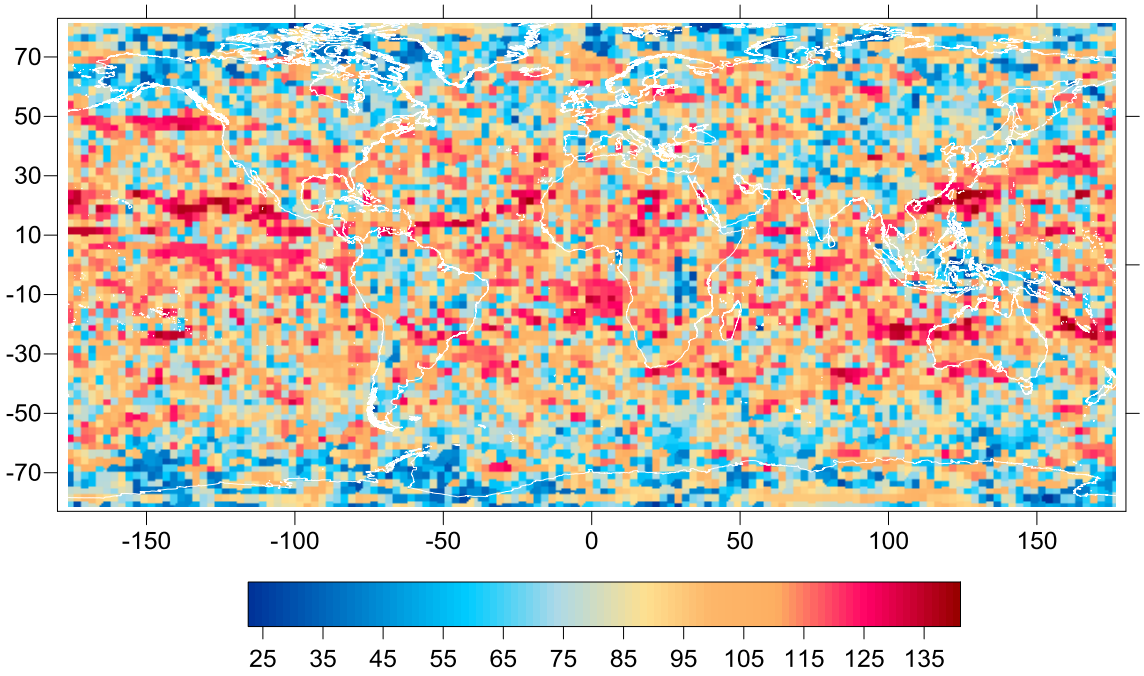

Fig.4 – Scale factor (C) of the adjusted Gaussian correlation function for ECMWF grid_2009_ZWD_Full, for cells of size 2.5°× 2.5°, in km.

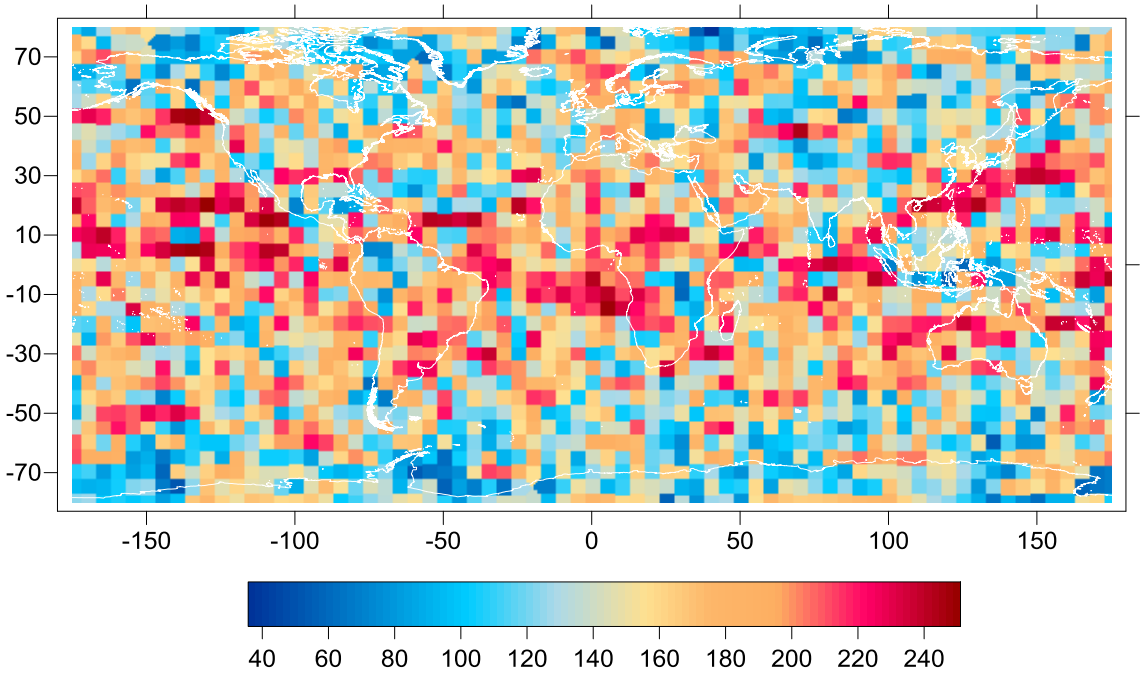

Fig.5 – Scale factor (C) of the adjusted Gaussian correlation function for ECMWF grid_2009_ZWD_Full, for cells of size 5°× 5°, in km.

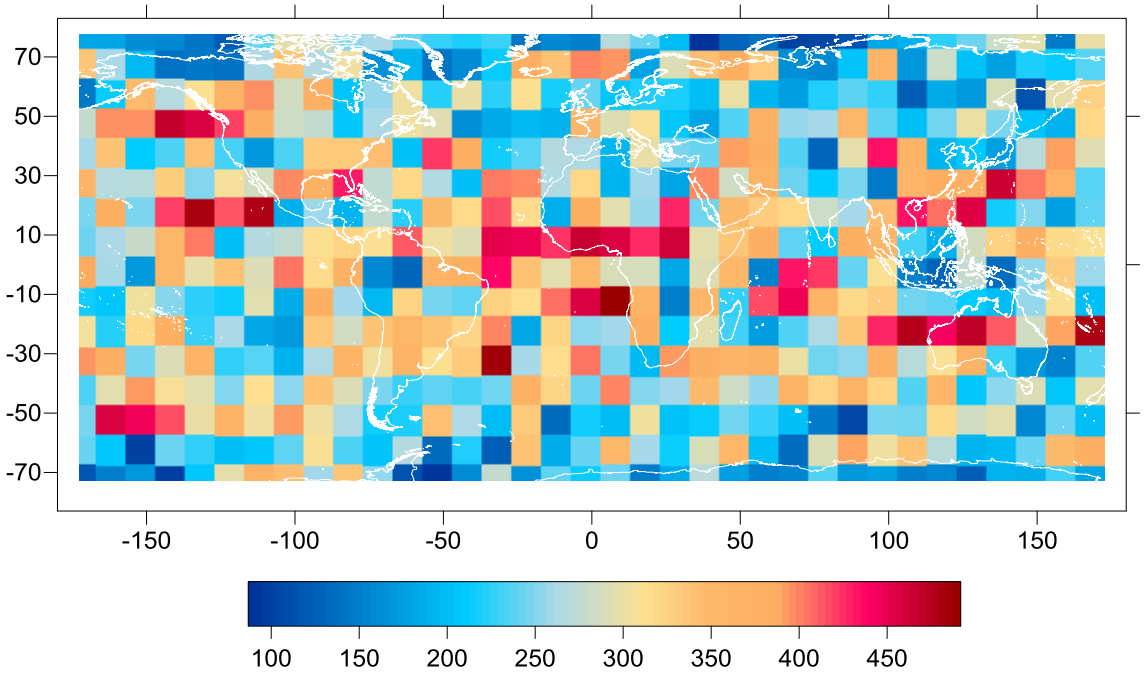

Fig.6 – Scale factor (C) of the adjusted Gaussian correlation function for ECMWF grid_2009_ZWD_Full, for cells of size 10°× 10°, in km.

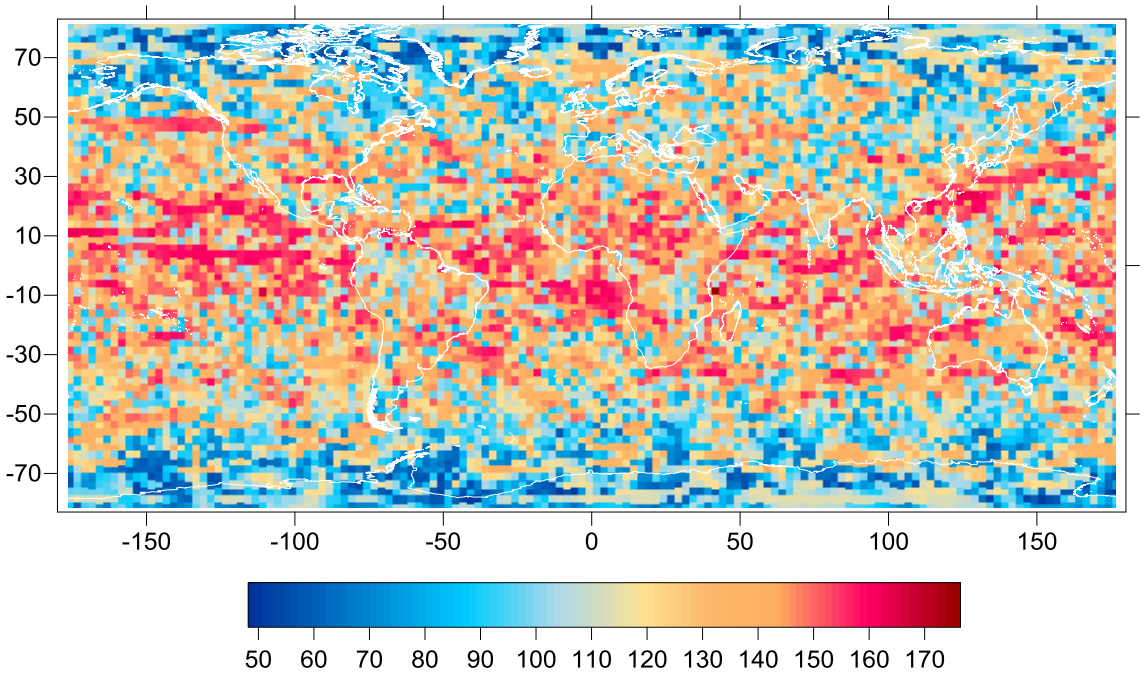

Fig.7 – Correlation scale (D) for ECMWF grid_2009_ZWD_Full, for cells of size 2.5°× 2.5°, in km.

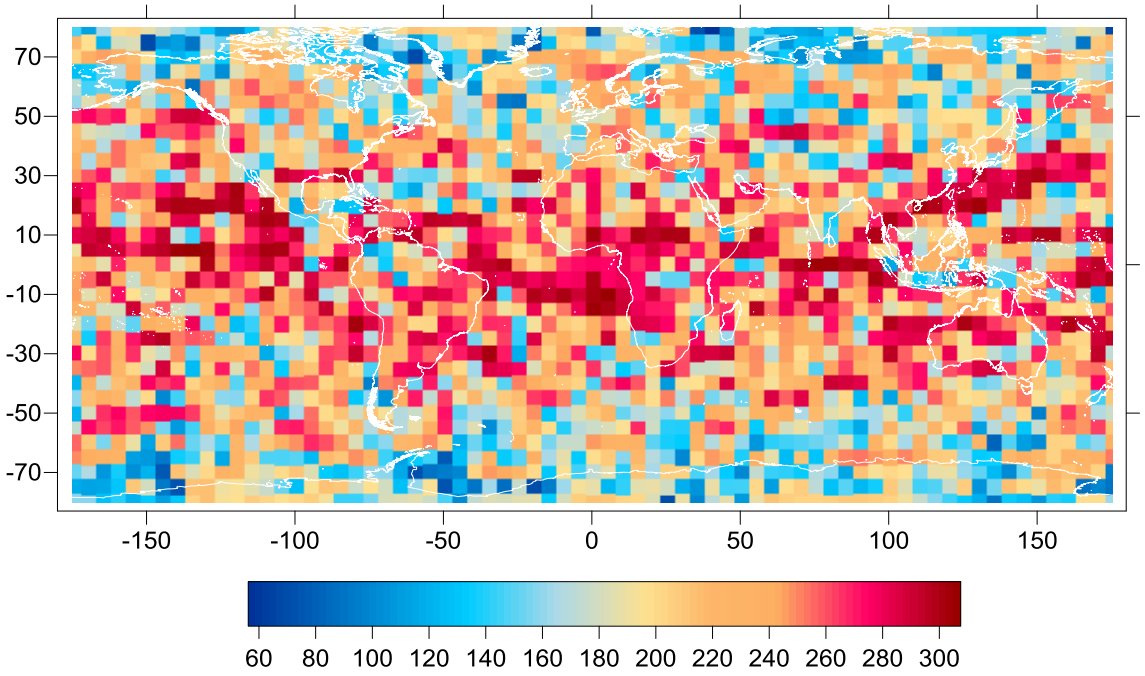

Fig.8 – Correlation scale (D) for ECMWF grid_2009_ZWD_Full, for cells of size 5°× 5°, in km.

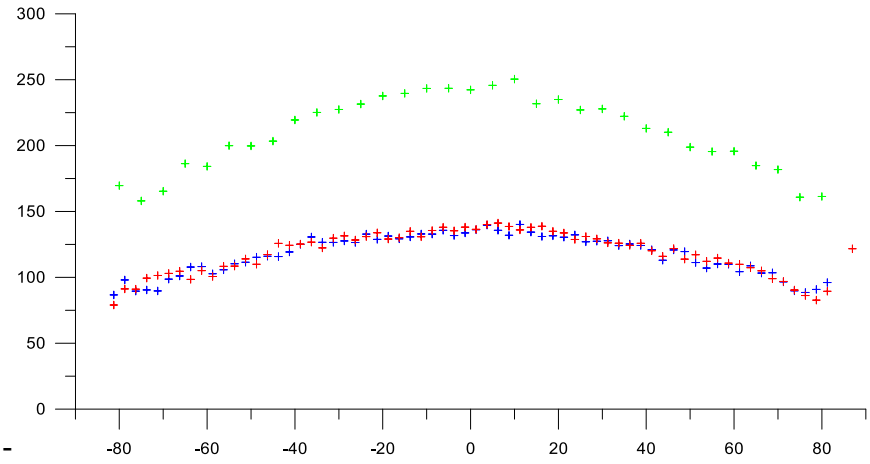

Fig.9 – Zonal mean Gaussian scale factor as function of latitude. Blue: results for grid_2009_ZWD_Full using cells of 2.5°× 2.5°; Green: results for grid_2009_ZWD_Full using cells of 5°× 5°; Red: results for a grid with the full ZWD field for 0h of 01/01/2008 using cells of 2.5°× 2.5°.

Another interesting result is that the scales have a slight dependence on latitude. To analyse this behaviour, the mean Gaussian scale factor of all cells at the same latitude (zonal mean) were computed and plotted in Figure 9.

Figures 10 and 11 represent two examples of the correlations and adjusted Gaussian function for two points located at different latitudes, using the cells of size 2.5°x2.5°. It can be observed that in most of the cases like these, a good Gaussian adjustment is obtained for the positive part of the correlation table. Figure 12 represents the Coefficient of Determination (R^2) of the adjustment of the scale factor C of the Gaussian function (1), for the same grid plotted in Figure 4. Although some cells exist for which the adjustment is not well

determined, the coefficient of determination is >0.9 for most of the cells with a mean value of 0.88 for all cells.

The dependence of the results on the size of the cells is not entirely surprising. When using cells of different sizes, different scales of variability are detected. As it can be observed on Figures 2 and 3, medium–large scales of size of hundreds of kilometres seem to be the dominant scales, both of the full and residual fields. However, these are not the scales of interest in the case of the GPD algorithm. In spite of the results obtained here, we know from experience that if large correlation scales and search domains are allowed, then the estimates will be influenced by a large number of observations, from a large region of influence, and the resulting wet tropospheric correction will become smoother as the size of the influence region and the correlation scale increase. In fact we know from experience that this type of algorithm might not be appropriate for the coastal regions, where we expect the ZWD field to vary at smaller scales. In particular, in the coastal regions, due to the shape of the coastline, it often happens that, for example two opposite sides of a narrow and mountainous island may have different atmospheric conditions, although being distant less than, for example, 100 km. In summary, although this study is inconclusive in various aspects, in face of the present results, we believe that the most realistic and appropriate scales to use in the GPD implementation are close to those obtained with cells of 2.5°x2.5°.

As a mixed result of this analysis and our experience with the GPD algorithm we presently adopted for the spatial correlation function of the ZWD field the same Gaussian function (1) with the following scale factor C: C=100 km for all latitudes in the band $|\text{latitude}| \leq 55°$ and C=70 km for $|\text{latitude}| > 55°$.

A theoretical quantification of the effect of a change in the correlation scale is not easy to perform. Each GPD estimate is a weighted average of the observations. The weight of each observation is function of its distance and time difference relative to the point of computation, of the spatial and temporal correlation scales, and of the white noise associated to each measurement. Therefore, varying the correlation scales will vary the weight of each observation and consequently the covariance matrix and the estimated value. The error of each estimate is also function of the covariance matrix and, therefore, of the adopted correlation scales. The impact of using different correlation scales has been quantified for Envisat cycle 58 by computing the difference between the GPD estimates using the following values for the scale factor C of the adopted Gaussian function: 1) C= 100 km everywhere and 2) C=100 km for all latitudes in the band $|\text{latitude}| \leq 55°$ and C=70 km for $|\text{latitude}| > 55°$. The statistics of the differences have a mean value of 0.3 mm and a standard deviation of 4.1 mm. The effect is only visible on a small number of points located at high latitudes as shown on figure 13.

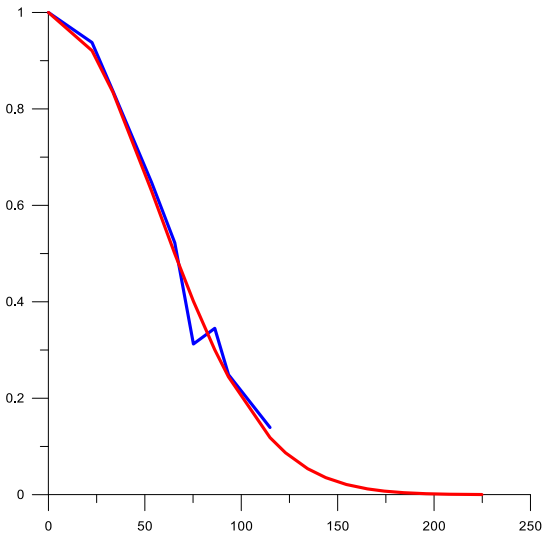

Fig.10 – Correlations (blue) and fitted Gaussian (red) for the cell of 2.5°× 2.5° centred on point of latitude 51.25° and longitude -26.25°.

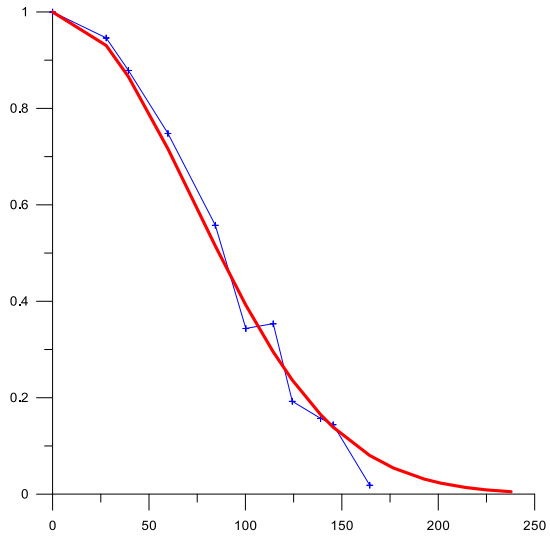

Fig.11 – Correlations (blue) and fitted Gaussian (red) for the cell of 2.5°× 2.5° centred on point of latitude 1.25° and longitude -26.25°.

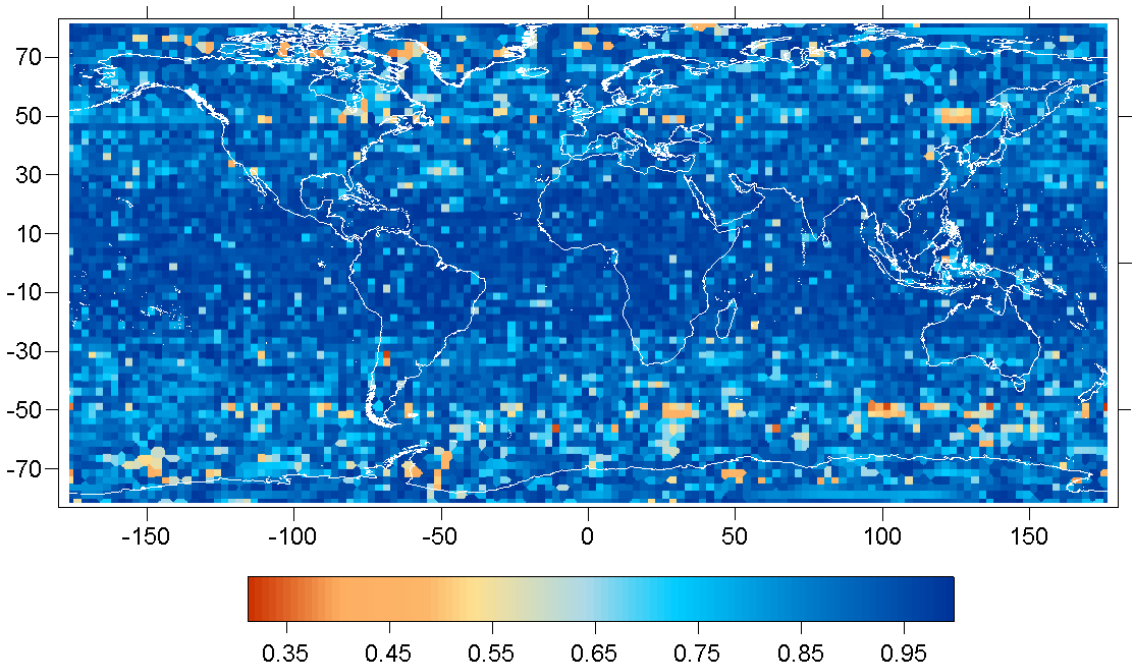

Fig.12 – Coefficient of Determination (R^2) of the adjustment of a Gaussian function to the correlation table of the grid shown on Figure 4.

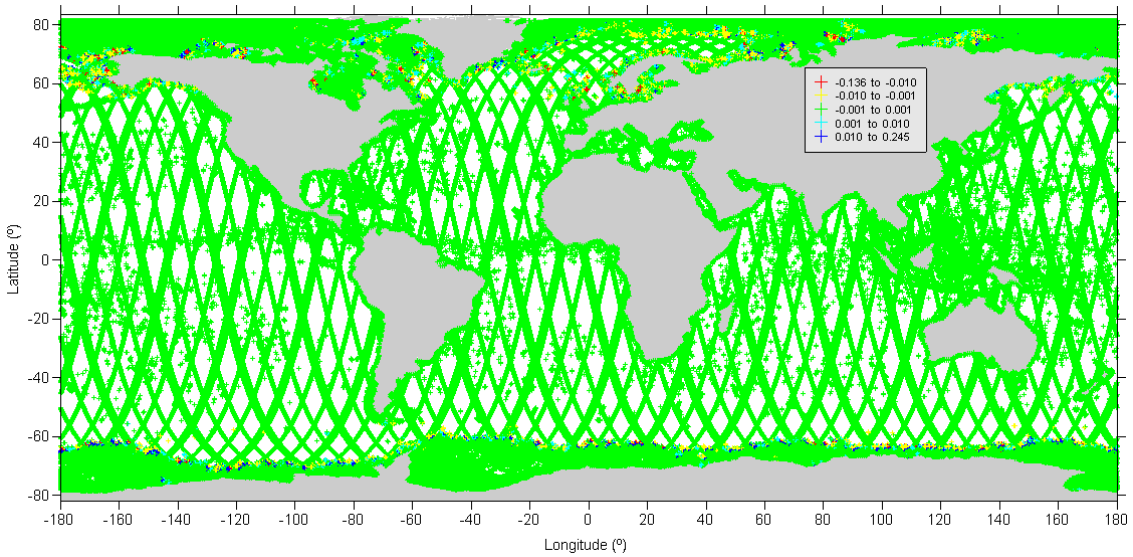

Fig.13 – Differences between the estimated GPD wet tropospheric correction using different spatial correlation scales (see text for details)

1.2.2 Determination of the 2-dimensional spatial correlation scale

A complementary assessment of the ZWD field autocorrelation was performed with software Matlab -- xcorr2.m routine -- over two ECMWF-derived ZWD global grids. The main objective of this approach was to conduct a two-dimensional spatial analysis of the autocorrelation, in order to assess not only the geographical impact on the correlation scale but also to gain some insight

into possible anisotropic behaviour of such scales. This is a similar procedure to that followed by Leewenburgh (2000) for sea level anomaly and sea surface temperature fields.

The results selected to be shown on this report refer to three different open-ocean test areas, centred at (-25º, 0º), (-45º, 30º) and (-25º, 50º), and around which 5ºx5º, 10ºx10º and 15ºx15º domains were considered. The variation of the dimension of the spatial domain aimed at the inspection of its influence on correlation length scale, but it also proved to be a valuable candidate for more detailed correlation anisotropy studies.

Prior to the ZWD field autocorrelation computation, several different attempts were conducted for de-trending the field. Two different strategies were adopted: (1) the removal of a least-square fitted 2D surface and (2) the removal of the mean temporal ZWD field. The remaining signal – de-trended or de-meaned, respectively – was the residual field being analysed.

The removal of the temporal mean field to the original one yields a ZWD "anomaly field", for which the analysis is performed. For the alternative option, that of a least-squares fitting de-trending, different surfaces were tested, being the 2nd degree surface adopted for all domains, irrespective of size or location. Figures 14 and 15 show an example of the 2D autocorrelation analysis performed over the two different residual ZWD fields obtained for the 5ºx5º domain centred at (-25º, 0º). Although this is not the most critical case, it already shows the subjectivity inherent to the choice of the de-trending surface. Different fitting surfaces will result for the same location when varying the dimension of the spatial domain thus yielding different residual ZWD fields. Therefore, not only does this procedure introduce a variable, domain-size dependent, influence on the field being analysed but it also makes it difficult to clearly state that this remaining signal is the one of relevance to the proposed study. Nevertheless, it can be argued that this procedure might succeed in removing most of the long scale signal of the field, making this a suitable approach for analysing the ZWD field features over small domains close to the coast. In fact, this fitting procedure showed to succeed, within the tested examples and methodologies, in minimizing the meridional spatial correlation scale variation with the domain size.

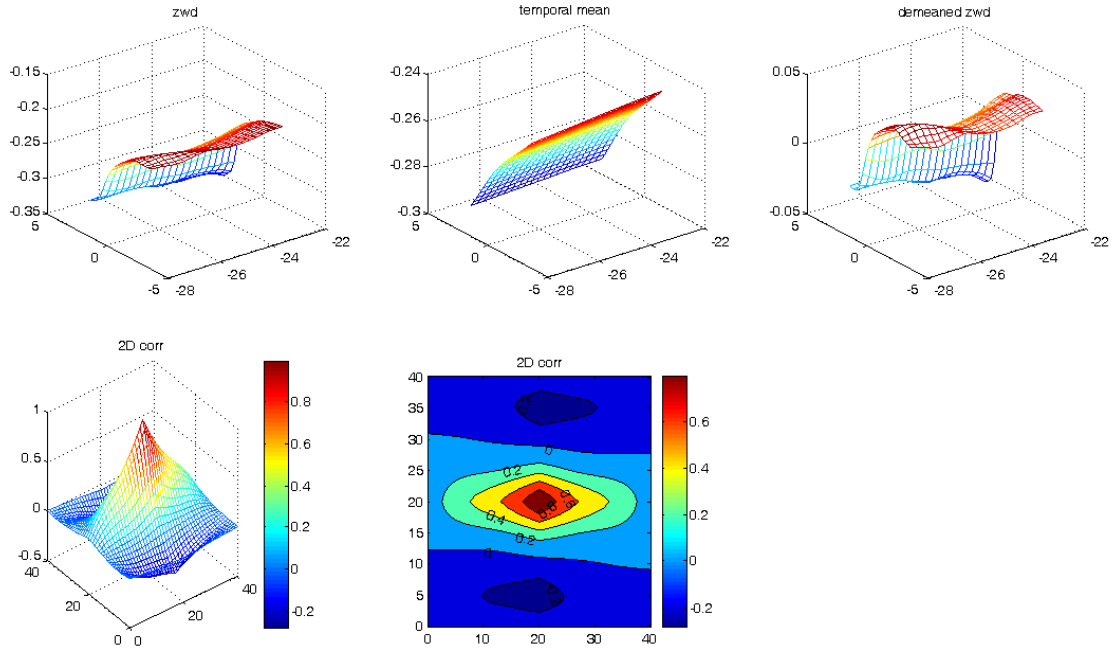

Fig.14 – 2D-correlation analysis for a 5°x5° domain centred at (-25°, 0°). Top, from left to right: ZWD field (in metres), mean temporal ZWD field (in metres), and the residual ZWD field, with horizontal axes in degrees. Bottom: 2D-autocorrelation of the residual ZWD field, with spatial axes in "pixels" (ECMWF grid points).

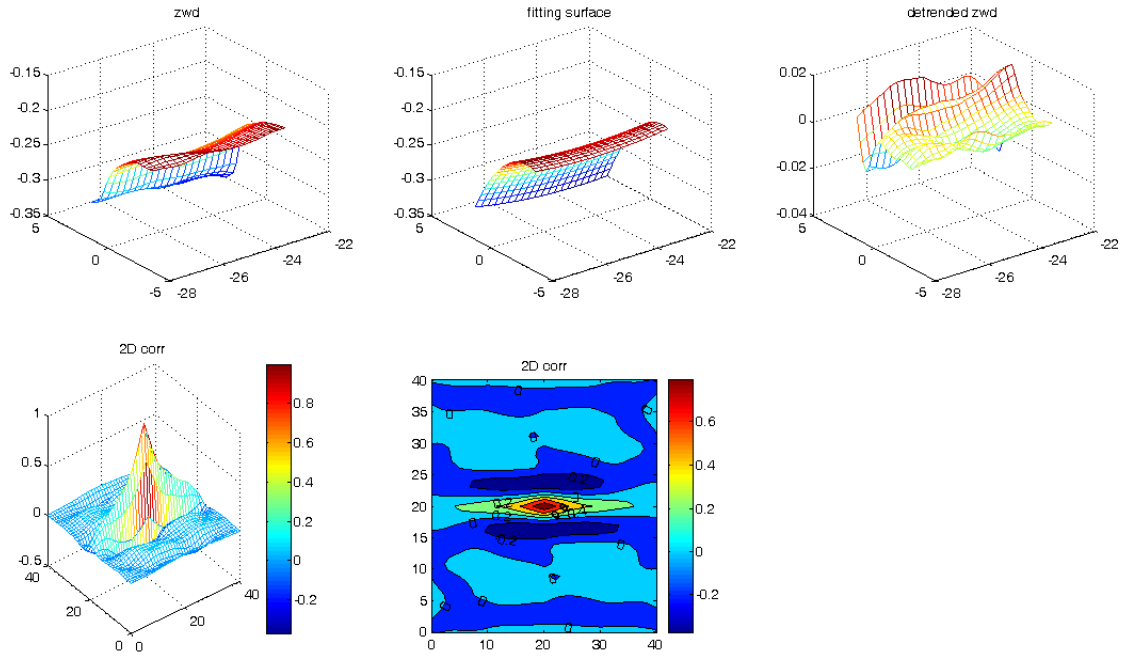

Fig.15 – 2D-correlation analysis for a 5°x5° domain centred at (-25°, 0°). Top, from left to right: ZWD field (in metres), 2nd degree least-squares fitted surface (in metres), and the de-trended ZWD field (in metres), with horizontal axes in degrees. Bottom: 2D-autocorrelation of the residual ZWD field, with spatial axes in "0.25° pixels" (ECMWF grid points).

Figures 16 and 17 show that the dimension of the sample area may also impact the anisotropy patterns found in the 2D-autocorrelation field, also raising some questions on whether meridional and zonal correlation length scales should always be the ones of concern or if, instead, minimum and maximum length scales, often occurring along near-elliptical patterns, should be inspected, and how.

The bottom plots in Figure 18 illustrate the possible influence an ad-hoc least squares fitting de-trending may have on the autocorrelation patterns. Here, the increase of the spatial domain's dimension strongly impacts not only the anisotropy but also the spatial orientation of the resulting autocorrelation features. Comparison with the analysis performed over both the original and the demeaned ZWD fields, where no relevant anisotropy patterns are to be found, irrespective of the domain's dimension, even suggests these features may be just artefacts of the de-trending procedure.

The analysis of the autocorrelation of the ZWD "anomaly" field revealed itself somehow inconclusive in what refers to the length scale that should be taken into account when performing an objective analysis procedure over ZWD fields. Overall, the 2D-autocorrelation field is such that the increase in the dimension of the spatial domain results in a nearly proportional "expansion" of the field and, consequently, of the length scale. Plus, no noticeable differences arise, apparently, with respect to the original ZWD field. The behaviour of the 2D-autocorrelation field does not present, apparently, any noticeable latitudinal dependency as well and, as mentioned above, the autocorrelation is, for most of the studied cases, almost isotropic. Except for the first example shown, in Figure 16, a visual inspection of the resulting autocorrelation surface suggests a positive 2D Gaussian function would best fit the results obtained. In this case, a spatial correlation scale could be obtained by fitting to this field a parabolic surface and taking the zero crossing distance as that length scale, as described in Pannekoucke et al. (2008).

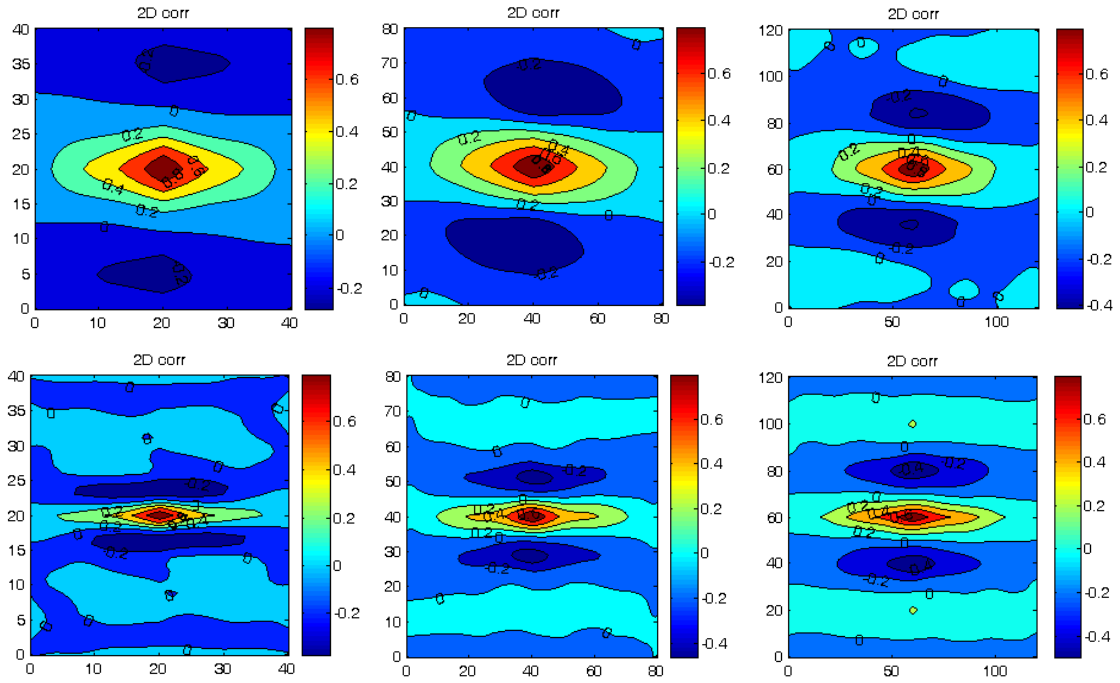

Fig.16 – 2D-correlation analysis for spatial domains centred at (-25°, 0°): 5°x5°, 10°x10° and 15°x15°, from left to right. Results for ZWD field (top), residual ZWD field (centre), and de-trended (with 2nd degree least-squares fitted surface) ZWD field (bottom). Spatial axes are in "0.25° pixels" units (ECMWF grid points).

This analysis clearly needs to be taken further than what was done in the scope of this study, being the main difficulties related with basic, yet very sensitive, steps that have to be taken prior to the computation of the autocorrelation of the ZWD field, namely: the choice of the most suitable de-trending procedure to be adopted, if any, and the decision regarding the dimension of the spatial domain that will encompass the scales that better characterise the features of the atmospheric field being analysed.

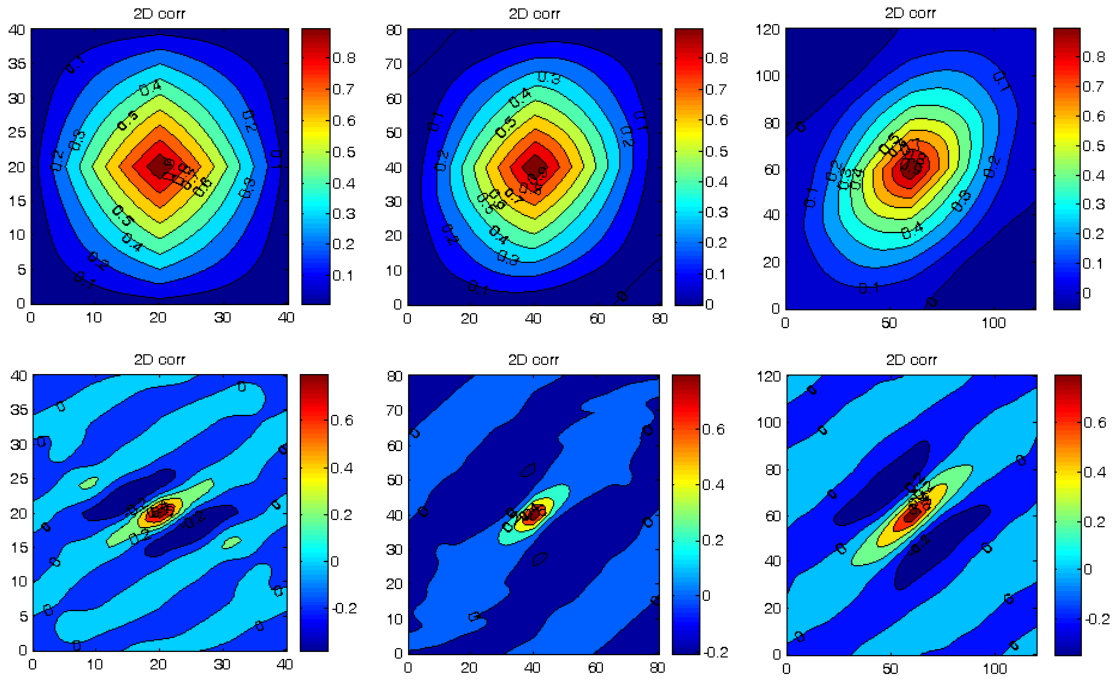

Fig.17 – 2D-correlation analysis for spatial domains centred at (-45°, 30°): 5°x5°, 10°x10° and 15°x15°, from left to right. Results for ZWD field (top), residual ZWD field (centre), and de-trended (with 2nd degree least-squares fitted surface) ZWD field (bottom). Spatial axes are in "0.25° pixels" units (ECMWF grid points).

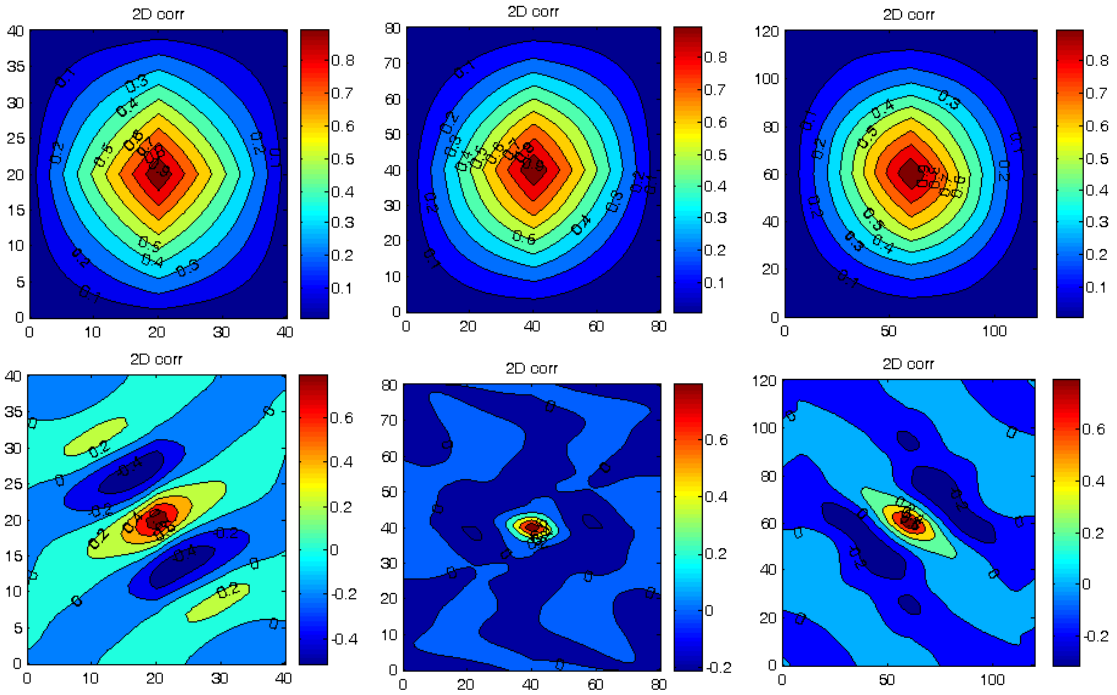

Fig.18 – 2D-correlation analysis for spatial domains centred at (-25°, 50°): 5°x5°, 10°x10° and 15°x15°, from left to right. Results for ZWD field (top), residual ZWD field (centre), and de-trended (with 2nd degree least-squares fitted surface) ZWD field (bottom). Spatial axes are in "0.25° pixels" units (ECMWF grid points).

2 GPD global validation

2.1 Introduction

If independent ground truth information were available on the tropospheric path delay in the coastal regions, the GPD output could be validated by comparison with such data. In the absence of ground truth information the GPD estimates are validated by inter-comparison with three data types: ZWD from the ALADIN model and from two algorithms also designed to compute wet tropospheric corrections in the coastal zone: the Mixed-Pixel Algorithm (MPA) (Brown, 2010) and the Land Proportion Algorithm (LPA) (Desportes et al., 2007). Sections 2.2 to 2.4 describe these data types. Section 2.5 presents an inter-comparison between all available ZWD fields for a set of Jason-2 cycles, since Jason-2 is the only satellite mission for which both the LPA and MPA algorithms are available.

2.2 ALADIN

ALADIN is an operational mesoscale numerical weather prediction model run by Météo-France. Despite being run over several different spatial domains, none of them is global, being the coverage focussed mainly on France and neighbouring countries (see Figure 19). The model provides, amongst many atmospheric parameters, surface pressure and temperature fields as well as humidity profiles on 15 pressure levels. The spatial resolution of ALADIN is 0.1º and grids are produced each 6 hours (ALADIN, 2009).

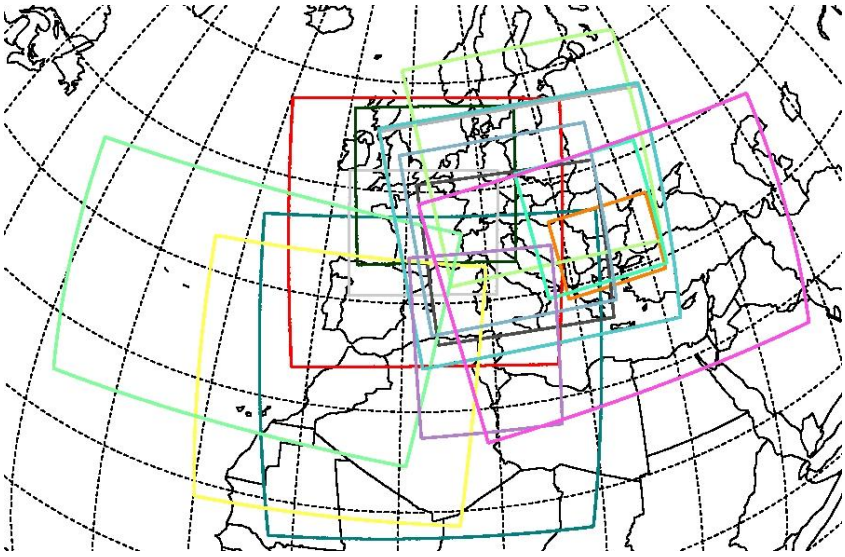

Fig.19 – Main spatial domains for which ALADIN is running (the red line limits the domain used within this study: -11° to 17° in longitude and 35° to 57° in latitude). (ALADIN, 2009)

The data fields used within this study for generating the ALADIN-derived wet tropospheric correction field were: Sea Surface Pressure (SLP), Surface Pressure (SurfP), 2-meter temperature (2T) and Total Column Water Vapour (TCWV). The ZWD calculation procedure was the same as for ECMWF, already described in [RD4].

The time coverage of the data acquired in the scope of COASTALT ranges from 09/02/2004 to 11/09/2009 – no column water vapour data are available prior to the beginning of this period. A land-sea mask – TERRE-MER -- and a relief map – ALTITUDE – were also provided together with the meteorological data.

2.3 The mixed-pixel algorithm

The MPA path delay (PD) retrieval algorithm developed at JPL (Jet Propulsion Laboratory) by Shannon Brown (2010), although also working for pure open-ocean scenes, it was specially designed to tackle the wet tropospheric correction retrieval for mixed land/ocean, i.e. coastal, altimetry data. The underlying motivations of this operationally simple and computationally fast algorithm are: (1) the fact that the PD retrieval is most sensitive to the difference between the two microwave radiometer (MWR) channels on and off of the 22-GHz water vapour absorption line (e.g. 18.7-GHz and 23.8-GHz channels for the JMR and AMR and 18.0-GHz and 21.0-GHz for the TMR) and (2) many of the error sources being common to each of those two MWR channels, errors correlated between them largely cancel in the retrieval process.

The MPA algorithm is based on the existing JMR / TMR / AMR open-ocean PD algorithm that is used for the altimeter GDR (Geophysical Data Record), described in Keihm et al. (1995):

$$PD_{GDR} = c_0\left(PD_0, WS_0\right) + \sum_f c_f\left(PD_0, WS_0\right)\log\left(280 - T_B(f)\right)$$

where the retrieval coefficients c_0 and c_f, are parameterised by first guess wind speed (WS_0) and PD (PD_0), T_B is the brightness temperature and the summation over f refers to the three MWR channels. For its use to be validly extended for coastal scenes, the algorithm coefficients are now parameterised by the land fraction at 18.7-GHz, $L_F^{18.7}$, taking thus the form (Brown, 2010):

$$PD_{MP} = c_0\left(PD_0, L_F^{18.7}\right) + \sum_f c_f\left(PD_0, L_F^{18.7}\right)\log\left(280 - T_B(f)\right)$$

The coefficients for the PD_{MP} algorithm are derived in a similar manner as those of the original PD_{GDR}. The algorithm is parameterized using a large database of simulated coastal brightness temperatures (T_B) observations along with the corresponding wet tropospheric PD. In practice, the PD_{MP} is used everywhere the land fraction is greater than 0.01 and the open-ocean PD algorithm, PD_{GDR}, is used everywhere the land fraction is zero -- threshold land fraction value was based on PD_{GDR} algorithm error evaluation -- being the two merged by linear interpolation for intermediate land fractions. The MPA is valid globally up to a

land fraction of 0.5, which corresponds to the antenna boresight centred on the coastline.

For operational use the algorithm requires only, in addition to the MWR measured T_B, an accurate land-sea mask. No dynamic ancillary data is needed, given that the database of modelled coastal land T_B is used for pre-processing purposes only. The method is suited for near-real-time processing and can be applied to any MWR to estimate integrated water vapour or wet PD in the coastal region, but the performance of the algorithm will depend upon the antenna pattern of the radiometer. Figures 20 to 22 illustrate the method's performance with AMR data. The MPA is currently applied to both JMR and AMR, being the algorithm error estimated to be, with respect to the latter, less than 0.8 cm up to 15 km from land, less than 1.0 cm within 10 km from land, less than 1.2 cm within 5 km from land, and less than 1.5 cm up to the coastline (Brown, 2010).

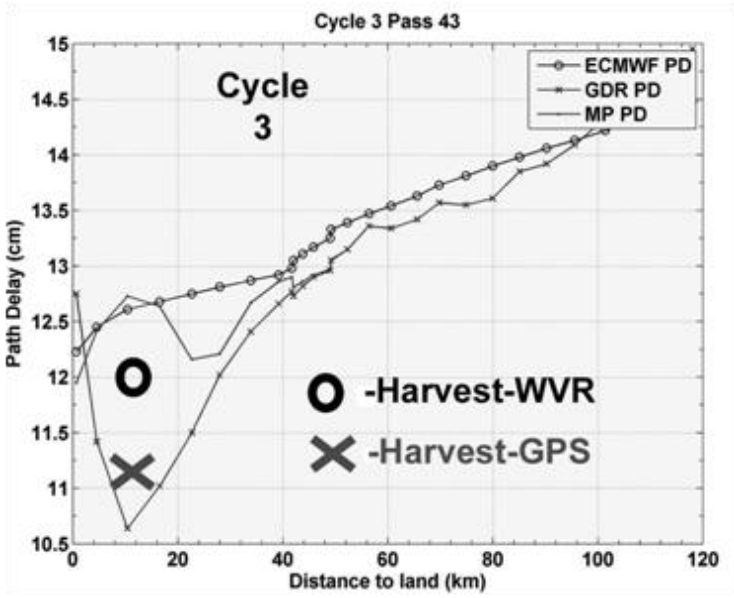

Fig.20 – AMR PD using standard GDR algorithm and MP algorithm for Jason-2 pass 43 at the Harvest oil platform, near (~10 km off) the California coast. The ECMWF model PD and that derived at Harvest from the GPS and water vapour radiometer (WVR) are also shown. (Brown, 2010)

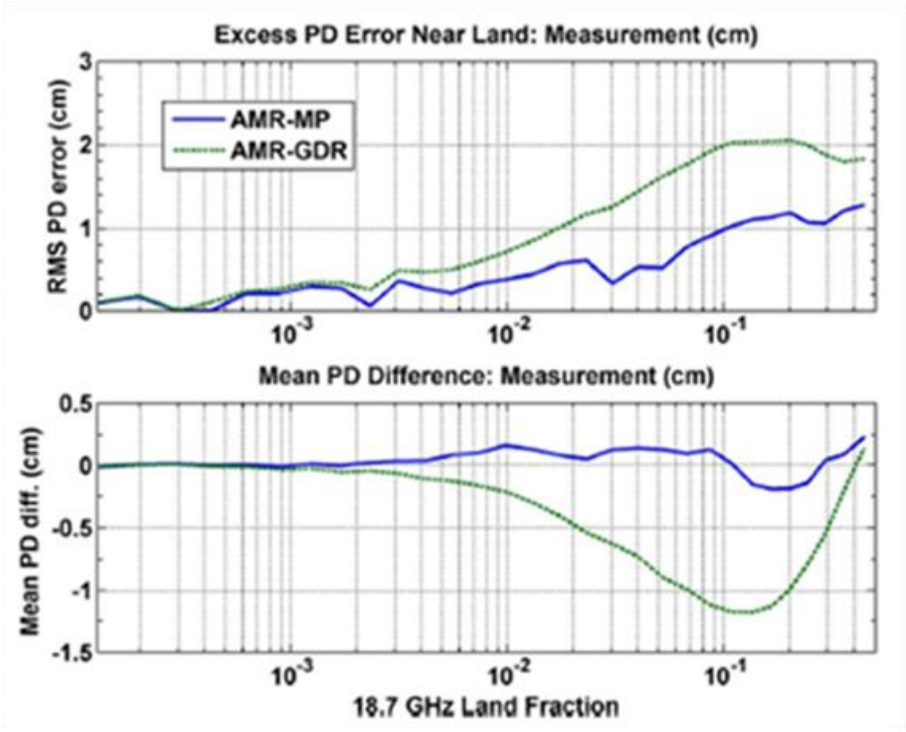

Fig.21 – Excess PD error near land estimated from the AMR minus ECMWF comparisons (top) and the bias approaching land. A 0.4-cm constant bias, equal to open-ocean mean difference between ECMWF and the AMR PDs, is subtracted from the mean differences to better illustrate the additional PD error near land. The comparisons include the algorithm error plus residual ECMWF model error in the coastal region. (Brown, 2010)

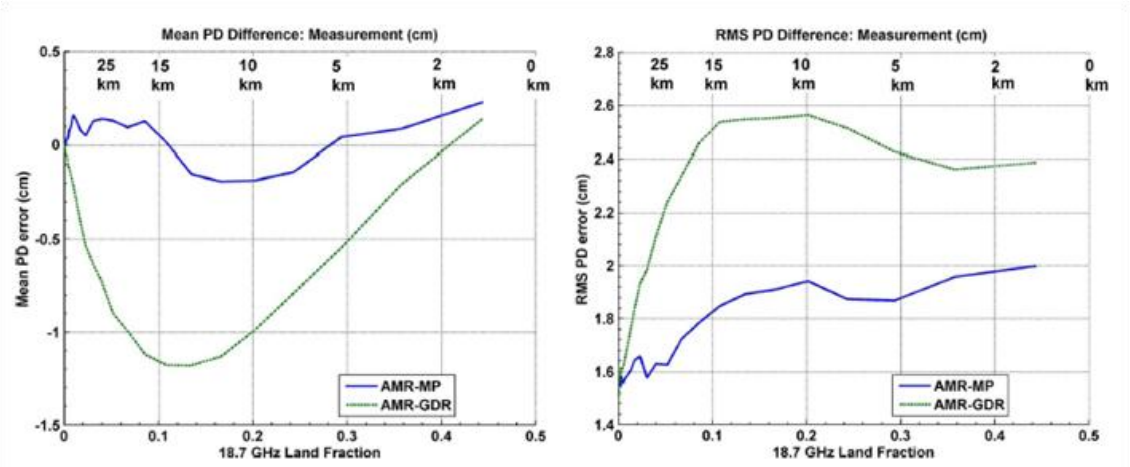

Fig.22 – Mean and rms of AMR minus ECMWF as a function of the 18.7-GHz land fraction (Brown, 2010).

The MPA implementations to Jason-1 and Jason-2 are available on RADS (Radar Altimetry Database System). The Jason-2 estimates were used in this study.

2.4 The Land-Proportion Algorithm

The wet tropospheric correction study developed by Desportes et al. (2007), is based on the removal of the land contamination from the MWR measured T_B values prior to their use in the pure open-ocean wet PD retrieval. Assumed all measurements are decontaminated from land influence, the oceanic algorithm used for JMR / TMR / AMR, can be used everywhere, up to the coast. This approach is similar to the one used by Bennartz (1999) to tackle the problem of mixed land/water measurements in SSM/I data by deriving the frequency-dependent fraction of land surface p within the MWR footprint in each measurement, from a high-resolution land-sea mask – 0.01º in this case. In addition to the MWR T_B measurements, this algorithm needs a database of coastal land T_B, which might prevent its global implementation on an operational basis.

The method used to correct the T_B is based on the correction function

$$\mathrm{corr}(p,f) = \left[T_{B\,land}(f) - T_{B\,sea}(f)\right] \times p\,(f)$$

where $T_{B\ land}$ and $T_{B\ sea}$ are estimated along the satellite ground track. For a complete sea-land transition, $T_{B\ sea}$ is the last pure oceanic T_B (the last MWR measurement for which p=0), and $T_{B\ land}$ is the first pure land T_B (p=1) - for incomplete transitions, the closest along-track T_B with p=0 or p=1 is taken.

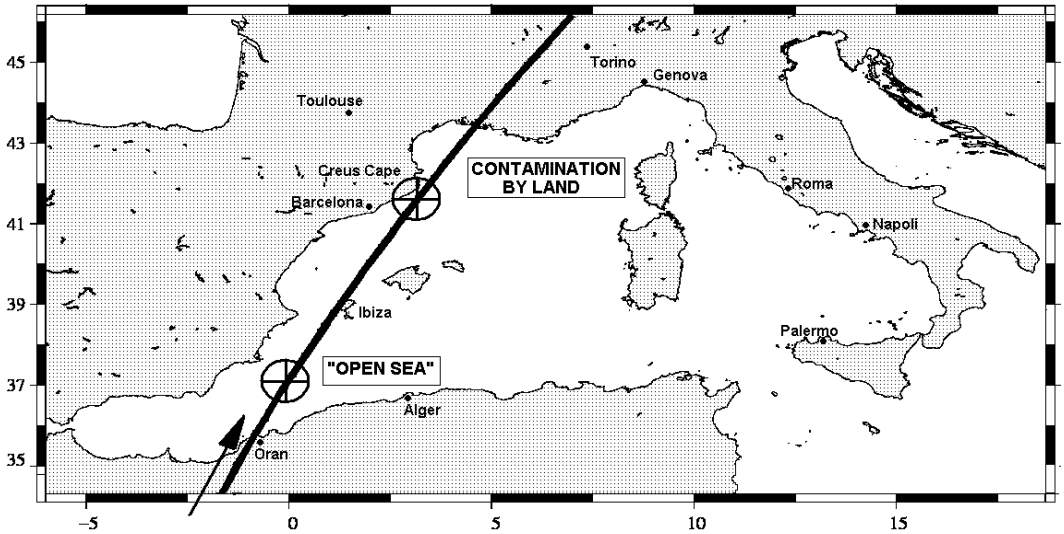

Fig.23 - (Top) TOPEX track number 187, 16 March around 12:00 (cycle 202) or 15 April around 06:00 (cycle 205). (Obligis et al., 2011)

When testing the algorithm, a linear dependency between the land proportion and the observed T_B was assumed. This is not, nonetheless, always valid, especially at 37 GHz, because of non-linearity of the atmospheric radiative transfer for atmosphere-sensitive channels. Discrepancies with respect to the mean linear dependency come from spatial variations of atmospheric humidity and also from along-track emissivity variations over sea and land (which are neglected within this method). The method also showed being quite sensitive to

the choice of $T_{B\,sea}$ and $T_{B\,land}$, especially when the satellite overpasses an island. Sensitivity studies were performed in TMR configuration (see Figure 23 for example), but the proposed methodologies are not dedicated to TOPEX (footprint diameter of 44.6, 37.4 and 23.5 km for the 18.0-, 21.0- and 37.0-GHz channels, respectively) but they are applicable to any other similar instruments onboard altimetry missions.

The performance of the method over real TMR data showed consistency with the results previously obtained over simulated data, as illustrated in Figures 24 and 25.

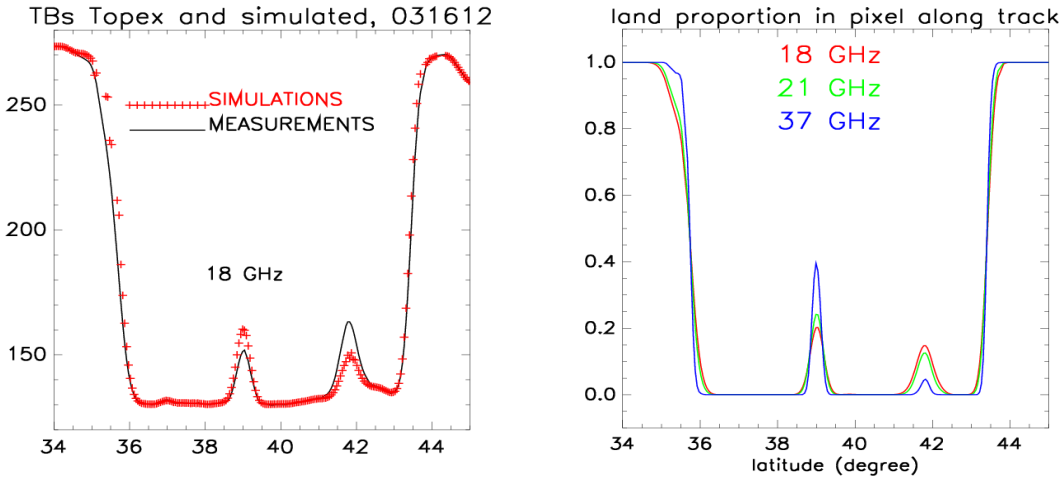

Fig.24- Land proportion in the footprint along the top figure track (left); Simulations compared to actual measurements on the same track (right). (Obligis et al. 2011)

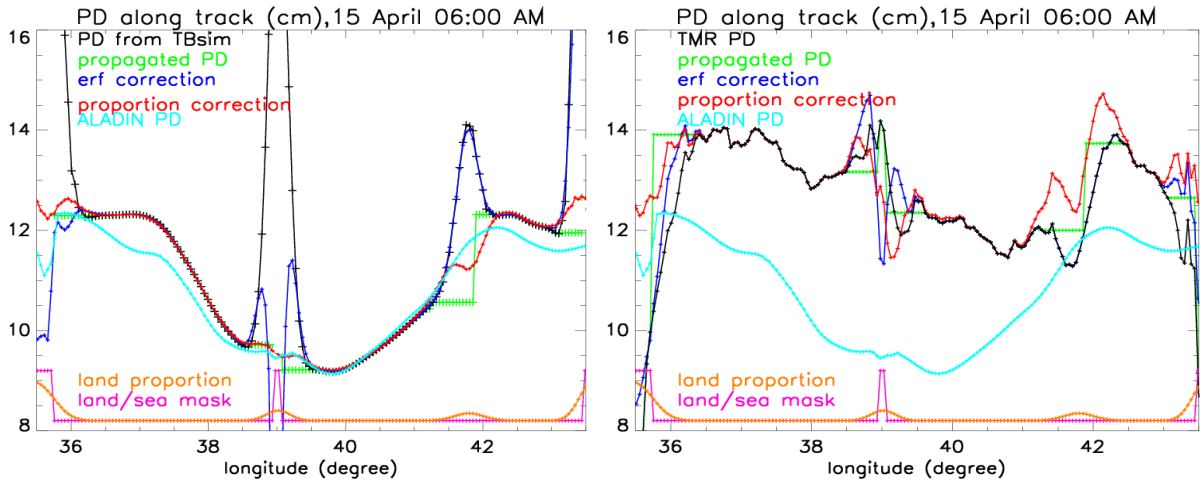

Fig.25 - Comparison between the wet PDs obtained from TB after different correction methods for T/P track 187 for simulated (left) and measured (right) TB values. The ALADIN PD shall not be regarded as an absolute reference, because of the existent negative bias with respect to TMR. (Obligis et al. 2011)

The LPA algorithm is being applied to Jason-2 data in the scope of project PISTACH. The data used in this study is the product made available on ftp://ftpsedr.cls.fr/pub/oceano/pistach/J2/IGDR/.

2.5 Inter-comparison between the various ZWD fields

For this study the GPD algorithm was run for a set of Jason-2 cycles, starting on cycle 3. The GPD implementation used here is the same as the one described in [RD4], adopting the spatial correlation scales as explained at the end of section 1.2.1. Although more cycles were computed, the analysis presented here is focused on Jason-2 cycles 3, 4 and 6. Cycle 5 was discarded since PISTACH data for this cycle revealed problems with many points with invalid MWR and LPA fields.

This section presents two types of comparisons:

A) Regional comparison, for the zone covered by the ALADIN model ($35° \leq \varphi \leq 57°$; $-11° \leq \lambda \leq 17°$) between the following ZWD fields:
   1. ECMWF (ECM)
   2. ALADIN (ALD)
   3. Original Microwave Radiometer correction (Wet_Rad))
   4. GPD
   5. MPA
   6. LPA

B) Global comparison between all the previous fields except the ALADIN model

We start by stating that, *a priori,* none of the mentioned fields can be considered as a reference field, that is, a field that can always be considered more accurate than all others. Therefore, this analysis, more than evaluating the accuracy of any of the ZWD estimates, allows detecting possible problems in the various data sets. Although not necessarily true, we assume that when most of the fields show a common trend, this shall be close to the true behaviour of the ZWD field. On the other hand, a field that shows large differences with respect to the majority of the others might be suspicious.

Tables 1 to 3 present the statistics of the comparison between all mentioned fields for Jason-2 cycles 3, 4 and 6, respectively. The first (non-shaded) rows refer to the global comparison. The shaded rows refer to the results for the ALADIN region. The statistics of each ZWD field and various differences between them are shown. In all cases only coastal points, that is, points for which all three coastal PD algorithms (GPD, MPA and LPA) were available, were selected for the comparisons.

As expected, the results for the ALADIN region reveal smaller differences between the various fields than the global results, since the wet tropospheric correction has moderate variability in the European region, compared with regions of larger variability as shown in Figure 6 of [RD4].

Considering the differences between the three coastal retrieval algorithms, MPA has a mean difference of about 3 mm with respect to GPD and LPA. This has nothing to do with the correction itself but rather to the fact that the Jason-2 wet tropospheric correction present on RADS have a small scale factor with respect to the corresponding values present in the PISTACH product. This is most probably due to the correction of detected anomalies in the Jason-2 channels, which is routinely updated in RADS but probably not in the PISTACH

processing. The GPD algorithm was run using the original MWR field present on PISTACH, which explains the mentioned differences.

The standard deviation of the differences between all three algorithms range from 10 to 15 mm, the closest retrievals being on average MPA and LPA. Although the differences are not statistically very significant, on average, GPD has differences with respect to the two models (ECMWF and ALADIN) smaller than MPA and LPA.

Figures 26 to 44 present the results for the full set of coastal points for cycle 6, in the ALADIN region. This set is composed by all points along the satellite ground tracks for which the wet tropospheric correction was retrieved by all three coastal PD algorithms. The horizontal axis represents point number as if we would join together all coastal track portions, without any gaps in between. This allows a complete vision of the fields for all coastal points of cycle 6 in the European region covered by ALADIN. Since there were many points and fields to represent, the set was divided in four parts, and only one part is represented in each figure. In addition, to allow a better inspection of the fields, for each region the two models (ECMWF and ALADIN) are shown in the top figure of each page and the three coastal algorithms are presented in the bottom figure of each page. Figures 26, 28, 30 and 32 show that the two models can have relatively large differences at the medium scale. The inspection of these differences in more detail show that ALADIN can reveal features that also depart significantly from the signals detected by the MWR in the open ocean. This is well illustrated in Figure 52, which represents pass 187 of cycle 3.

Figures 34 to 38 show the Differences between GPD and each of the other analysed corrections, in metres, for Jason 2 cycle 6, over the European region covered by the ALADIN model. Figures 39 to 43 show the histograms of the differences between GPD and each of the other corrections, in metres, for the same Jason 2 cycle, over the same European region covered by the ALADIN model.

Figures 27, 29, 31 and 33 show that, overall, the three coastal PD algorithms show a common behaviour in most of the regions. However, there are tracks were the differences between the various corrections can reach several centimetres.

Figures 44 to 47 show the global results corresponding to the same differences shown in figures 34 to 37. Overall these two group of figures and the histograms on figures 39 to 43 confirm and illustrate the results presented in the statistics shown in Tables 1 to 3 and the along track plots of figures 26 to 33

Figure 48 shows the location of three passes (20, 156 and 187) for which the results are shown in Figures 49 to 52. Figures 49 and 51 show examples of two passes were the coastal fields may reveal significant differences and where, in general, the influence of- the closest GNSS stations can be seen on GPD. Figure 50 illustrates one pass (146) for which the differences between the three coastal algorithms are larger. This corresponds to the region after point 700 on Figures 28 and 29. The same extreme differences can be seen in Figures 35 and 36 over the same pass between Great Britain and Ireland.

Tab.1 – Statistics of the comparison between the various ZWD fields (see text for details) for Jason-2 cycle 3. First set of rows refer to global comparison; grey shaded cells refer to the regional comparison for the ALADIN region. Values are millimetres.

FIELD	Np	Mean	sigma	Min	max
wet_Rad	25290	-164.9	100	-599	0
GPD	25290	-172.2	98.9	-629	11
MPA	25290	-169.4	97.6	-499	-1
LPA	25290	-171.6	98.2	-531	0
ECM	25290	-175.9	100.2	-463	-4
GPD-MPA	25290	-2.8	16.0	-549	108
GPD-LPA	25290	-0.6	14.9	-545	238
MPA-LPA	25290	2.2	12.5	-107	221
ECM-GPD	25290	-3.6	13.4	-112	542
ECM-MPA	25290	-6.4	17.5	-97	128
ECM-LPA	25290	-4.2	16.9	-128	174
wet_Rad	1582	-155.2	36.4	-272	-43
GPD	1582	-165.2	36.8	-290	-57
MPA	1582	-162.3	34.3	-278	-52
LPA	1582	-165.7	33.7	-265	-61
ECM	1582	-169.3	35.7	-262	-70
ALD	1582	-166.5	36.3	-275	-70
GPD-MPA	1582	-2.9	13.5	-106	71
GPD-LPA	1582	0.5	12.4	-49	98
MPA-LCA	1582	3.4	10.3	-54	94
ECM-GPD	1582	-4.1	13.0	-49	79
ECM-MPA	1582	-7	15.1	-88	66
ECM-LPA	1582	-3.6	13.9	-49	51
ALD-GPD	1582	-1.2	18.3	-78	106
ALD-MPA	1582	-4.1	18.9	-90	93
ALD-LPA	1582	-0.7	18.1	-85	77

Tab.2 – Statistics of the comparison between the various ZWD fields (see text for details) for Jason-2 cycle 4. First set of rows refer to global

comparison; grey shaded cells refer to the regional comparison for the ALADIN region. Values are millimetres.

FIELD	np	Mean	sigma	Min	Max
wet_Rad	25174	-165.9	100.4	-661	0
GPD	25174	-173.3	98.9	-502	193
MPA	25174	-169.9	98	-499	-1
LPA	25174	-172.4	99	-678	0
ECM	25174	-176.5	99.7	-440	-6
GPD-MPA	25174	-3.4	15.0	-194	261
GPD-MPA	25174	-0.9	14.6	-169	253
MPA-LCA	25174	2.5	12.6	-145	339
ECM-GPD	25174	-3.2	12.8	-219	200
ECM-MPA	25174	-6.6	17	-127	156
ECM-LPA	25174	-4.1	16.9	-151	269
wet_Rad	1541	-147.1	34.5	-270	-63
GPD	1541	-156.1	34.1	-274	-18
MPA	1541	-153.3	33.5	-268	-79
LPA	1541	-156.5	33.2	-276	-80
ECM	1541	-159.6	34.6	-278	-91
ALD	1541	-156.5	35.2	-271	-85
GPD-MPA	1541	-2.8	12.7	-60	92
GPD-MPA	1541	0.4	12	-52	90
MPA-LPA	1541	3.2	9.4	-61	68
ECM-GPD	1541	-3.5	11.7	-87	39
ECM-MPA	1541	-6.3	14.4	-65	51
ECM-LPA	1541	-3.1	13.6	-63	37
ALD-GPD	1541	-0.4	15.9	-87	50
ALD-MPA	1541	-3.2	17	-71	46
ALD-LPA	1541	0	16.4	-62	57

Tab.3 – Statistics of the comparison between the various ZWD fields (see text for details) for Jason-2 cycle 6. First set of rows refer to global

comparison; grey shaded cells refer to the regional comparison for the ALADIN region. Values are millimetres.

FIELD	np	Mean	sigma	Min	max
wet_Rad	24547	-166	107.7	-610	0
GPD	24547	-172.2	106.7	-609	-3
MPA	24547	-168.9	104.5	-500	-1
LPA	24547	-172.1	105.6	-546	0
ECM	24547	-174.9	106.7	-433	-3
GPD-MPA	24547	-3.3	16.8	-228	157
GPD-MPA	24547	0	15.3	-217	166
MPA-LPA	24547	3.2	13.8	-132	278
ECM-GPD	24547	-2.8	14.3	-111	203
ECM-MPA	24547	-6	18.5	-160	194
ECM-LPA	24547	-2.8	18.4	-136	203
wet_Rad	1495	-152.3	42.9	-290	-51
GPD	1495	-160.1	39.4	-252	-75
MPA	1495	-156.9	41.4	-283	-70
LPA	1495	-161.8	41.7	-278	-70
ECM	1495	-162.3	39.8	-257	-79
ALD	1495	-159.4	38.7	-259	-63
GPD-MPA	1495	-3.2	15.7	-84	101
GPD-LCA	1495	1.7	14.2	-42	96
MPA-LPA	1495	4.8	12.3	-31	102
ECM-GPD	1495	-2.2	11.1	-81	25
ECM-MPA	1495	-5.4	17.2	-71	109
ECM-LPA	1495	-0.5	15.8	-59	103
ALD-GPD	1495	0.7	13.9	-68	43
ALD-MPA	1495	-2.4	18.3	-73	113
ALD-LPA	1495	2.4	17.5	-70	105

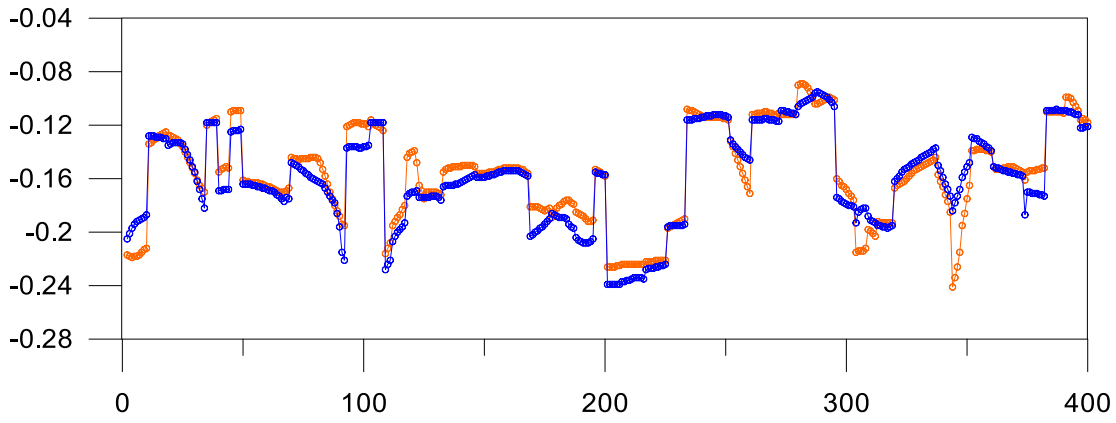

Fig.26 – ZWD from ECMWF (blue) and ALADIN (orange) for the first 400 coastal points of Jason-2 cycle 6 (passes 1 to 87). x axis is along track point number, by ascending time order.

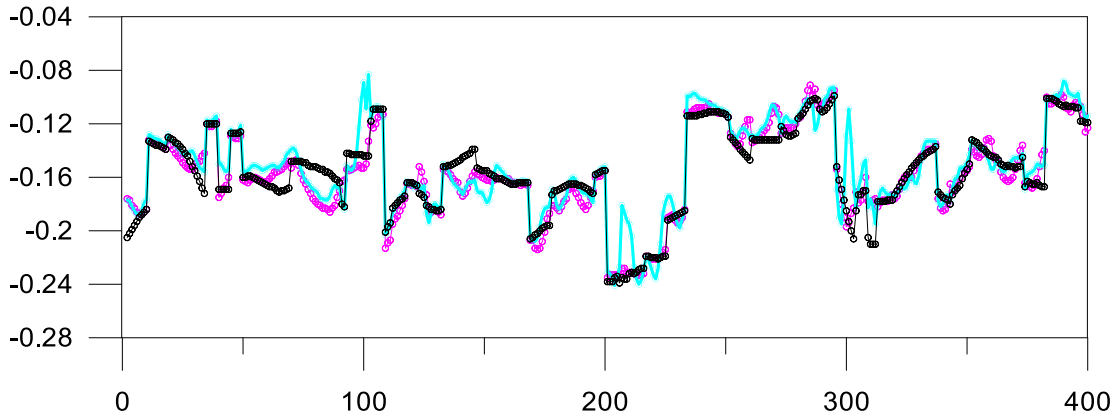

Fig.27 – ZWD from GPD (black), MPA (cyan) and LPA (pink) algorithms for the first 400 coastal points of Jason-2 cycle 6 (passes 1 to 87). x axis is along track point number, by ascending time order.

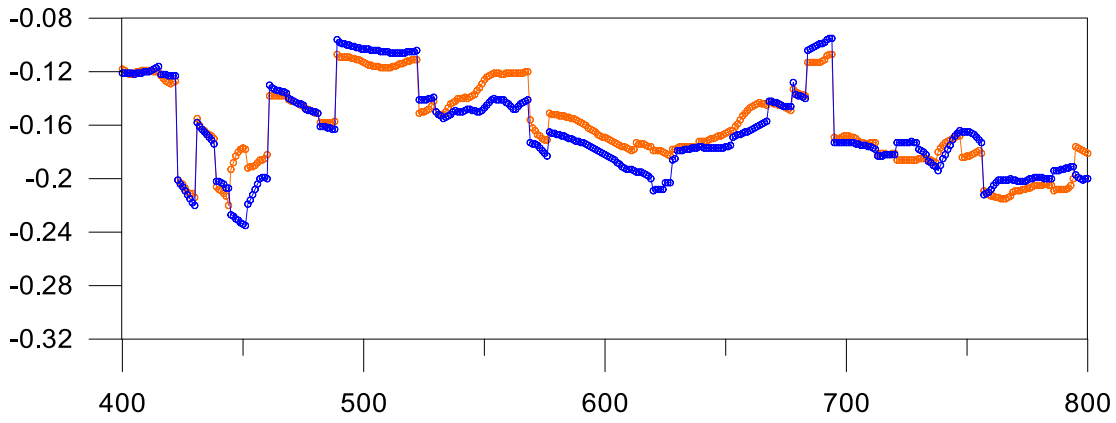

Fig.28 – ZWD from ECMWF (blue) and ALADIN (orange) for coastal points 400 to 800 of Jason-2 cycle 6 (passes 87 to 161). x axis is along track point number, by ascending time order.

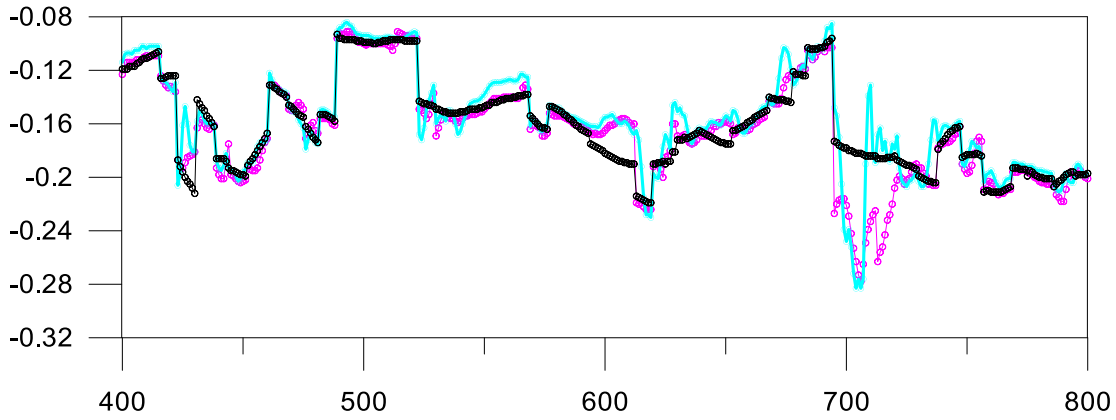

Fig.29 – ZWD from GPD (black), MPA (cyan) and LPA (pink) algorithms for coastal points 400 to 800 of Jason-2 cycle 6 (passes 87 to 161). x axis is along track point number, by ascending time order.

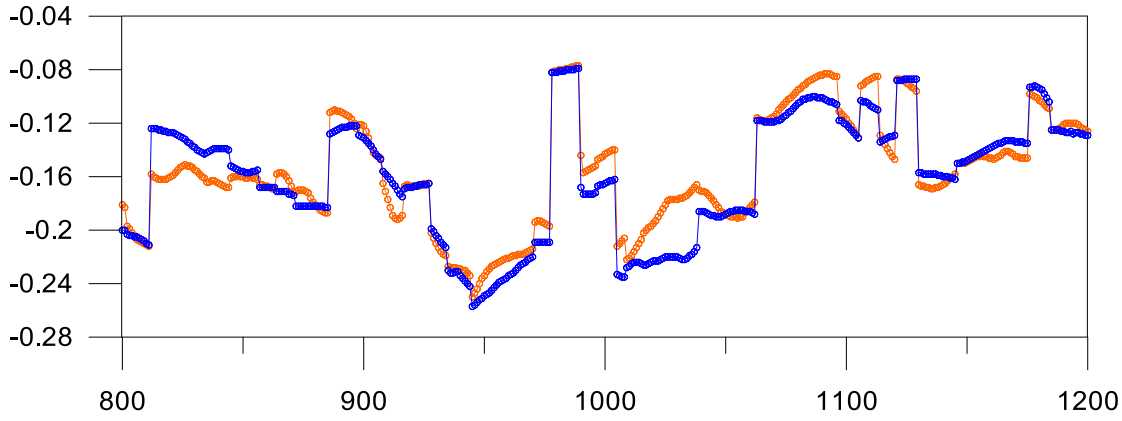

Fig.30 – ZWD from ECMWF (blue) and ALADIN (orange) for coastal points 800 to 1200 of Jason-2 cycle 6 (passes 161 to 222). x axis is along track point number, by ascending time order.

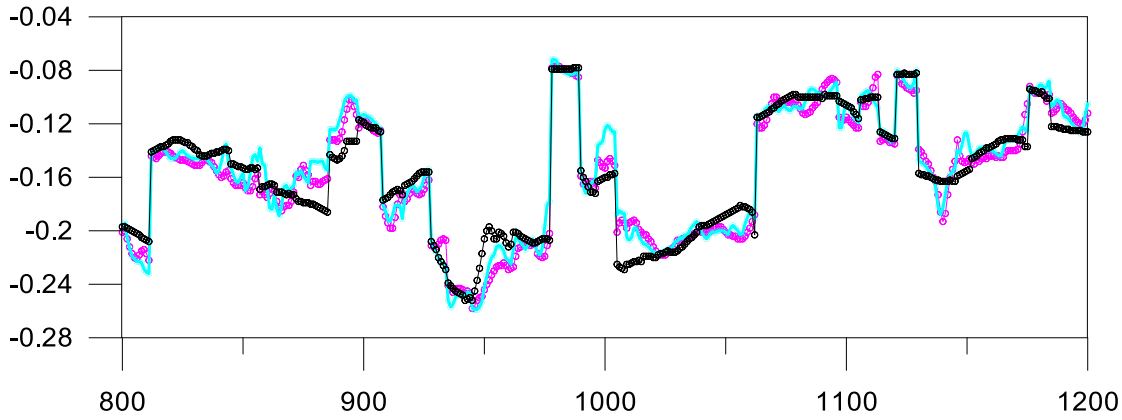

Fig.31 – ZWD from GPD (black), MPA (cyan) and LPA (pink) algorithms for coastal points 800 to 1200 of Jason-2 cycle 6 (passes 161 to 222). x axis is along track point number, by ascending time order.

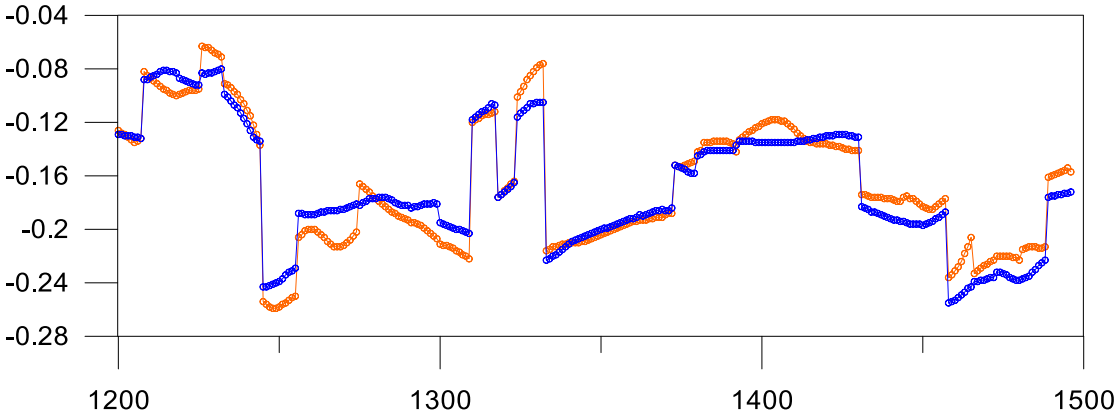

Fig.32 – ZWD from ECMWF (blue) and ALADIN (orange) for coastal points 1200 to 1500 of Jason-2 cycle 6 (passes 222 to 248. x axis is along track point number, by ascending time order.

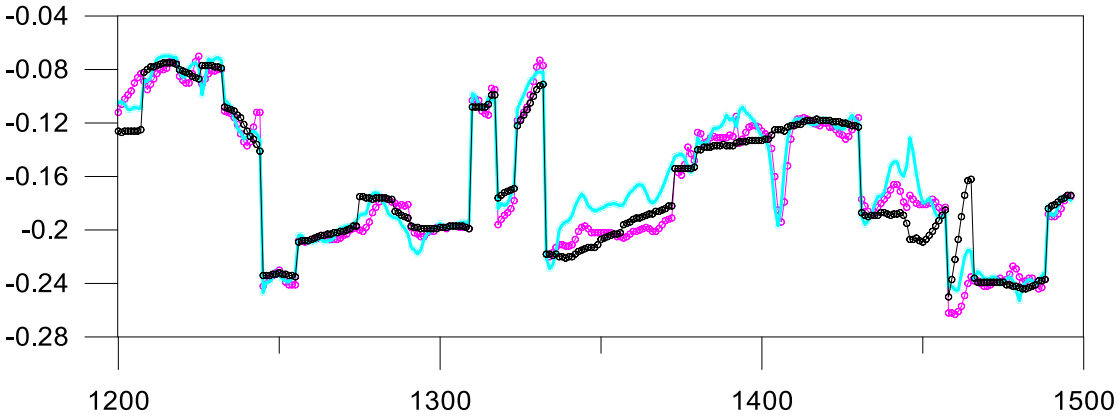

Fig.33 – ZWD from GPD (black), MPA (cyan) and LPA (pink) algorithms for coastal points 1200 to 1500 of Jason-2 cycle 6 (passes 222 to 248). x axis is along track point number, by ascending time order.

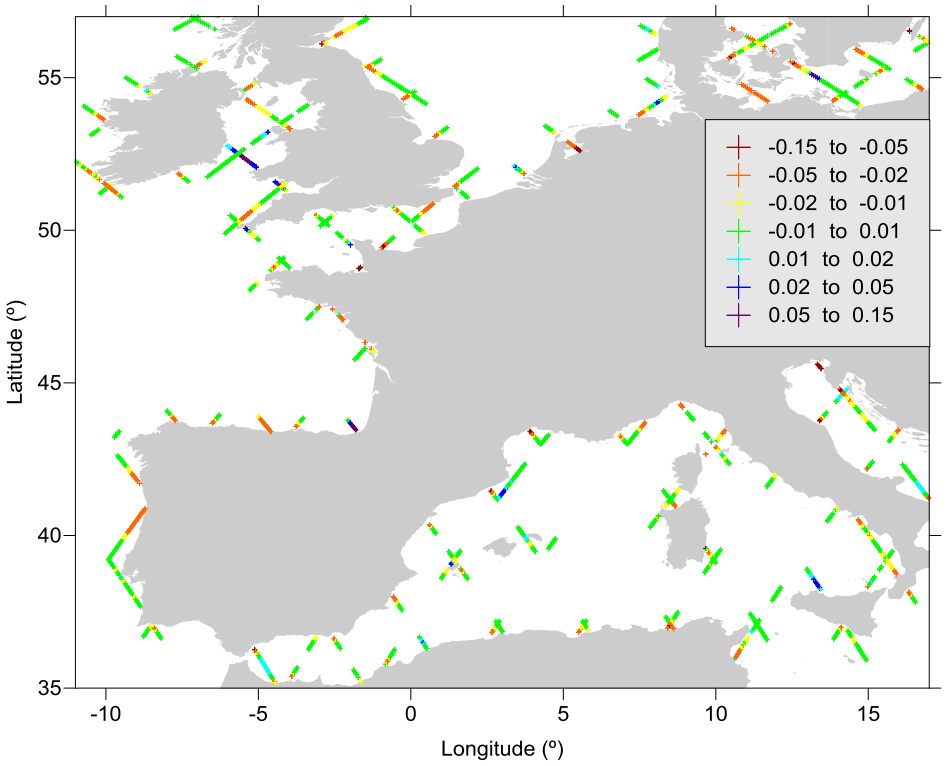

Fig.34 – Differences between GPD and MWR corrections, in metres, for Jason-2 cycle 6, over the European region covered by the ALADIN model.

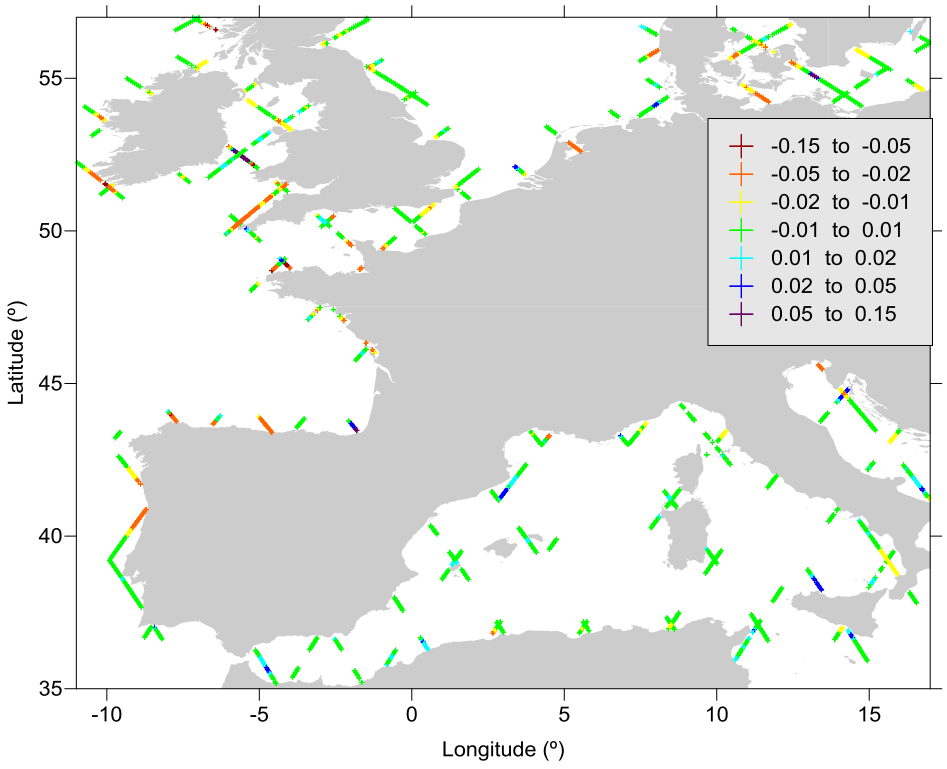

Fig.35 – Differences between GPD and MPA corrections, in metres, for Jason-2 cycle 6, over the European region covered by the ALADIN model.

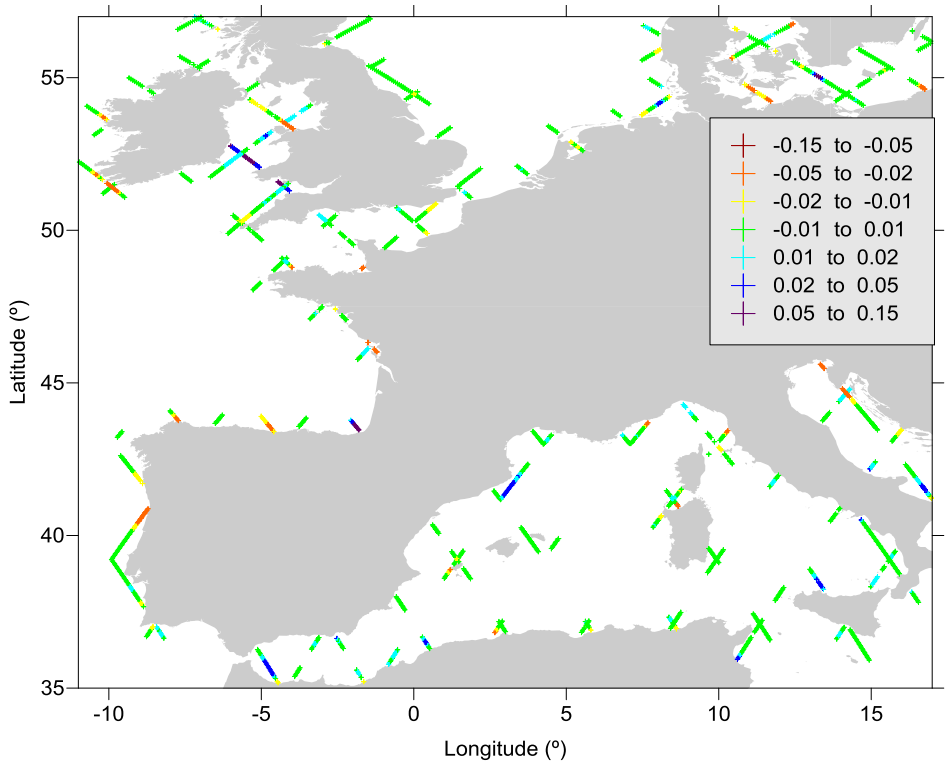

Fig.36 – Differences between GPD and LPA corrections, in metres, for Jason-2 cycle 6, over the European region covered by the ALADIN model.

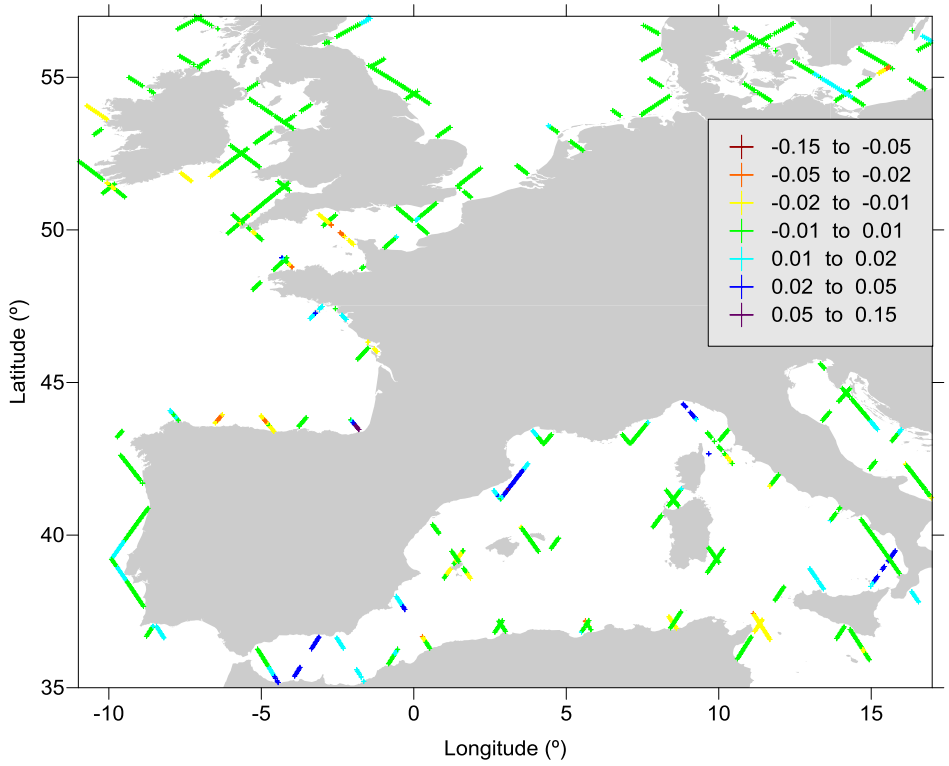

Fig.37 – Differences between GPD and ECMWF corrections, in metres, for Jason-2 cycle 6, over the European region covered by the ALADIN model.

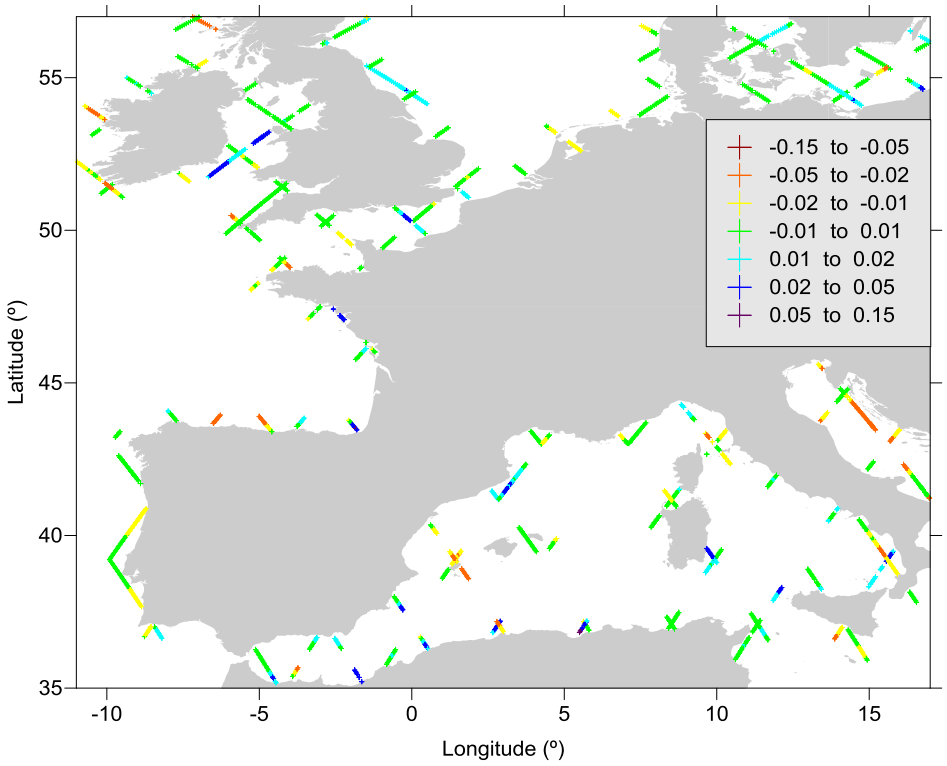

Fig.38 – Differences between GPD and ALADIN corrections, in metres, for Jason-2 cycle 6, over the European region covered by the ALADIN model.

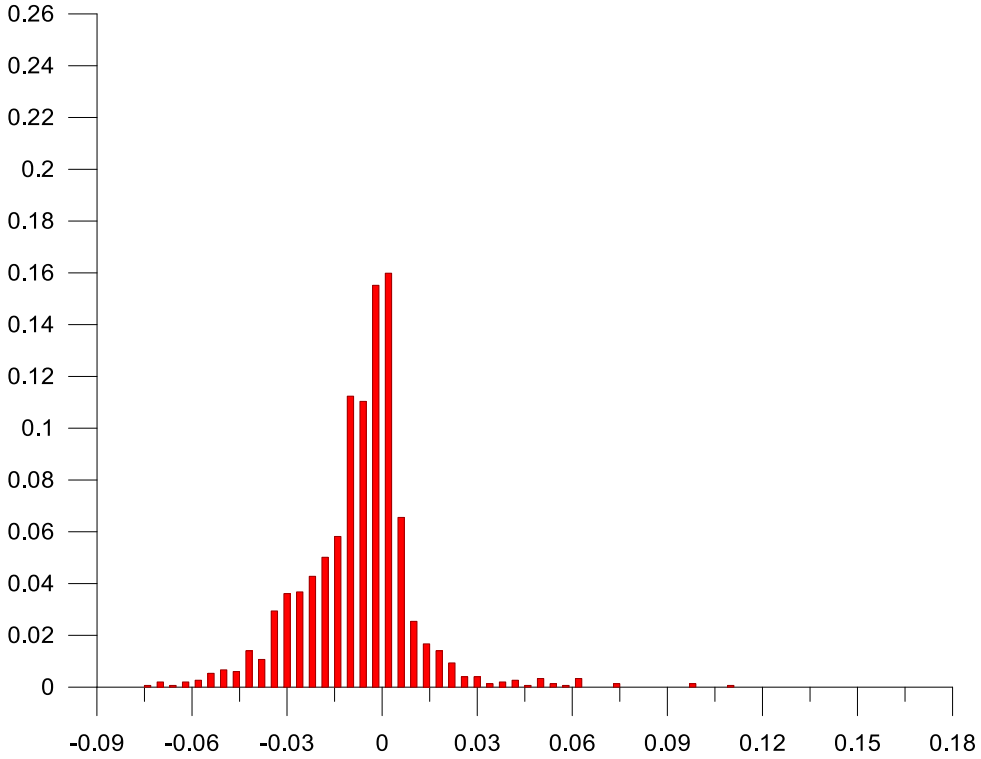

Fig.39 – Histogram of the differences between GPD and MWR corrections, in metres, for Jason-2 cycle 6, over the European region covered by the ALADIN model.

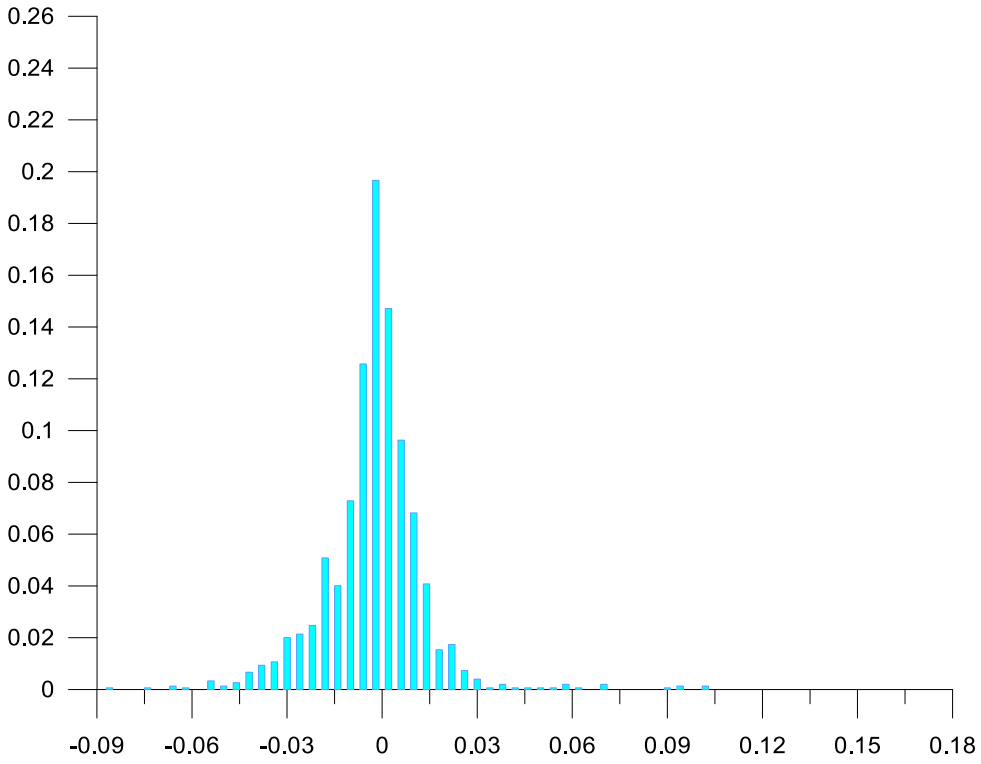

Fig.40 – Histogram of the differences between GPD and MPA corrections, in metres, for Jason-2 cycle 6, over the European region covered by the ALADIN model.

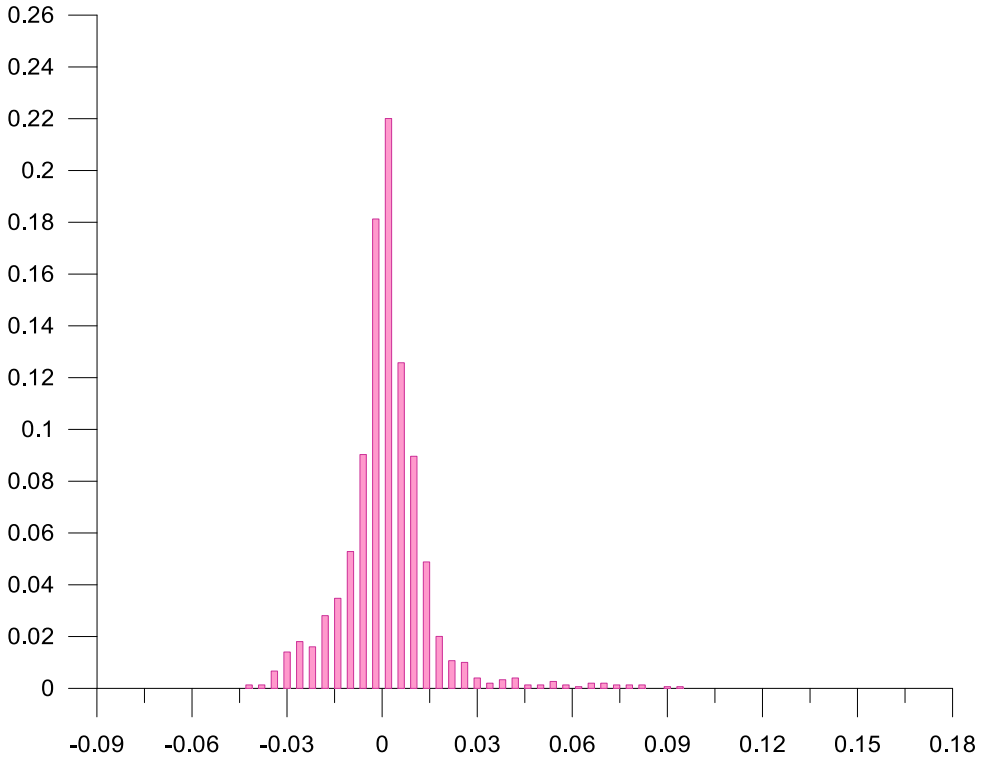

Fig.41 – Histogram of the differences between GPD and LPA corrections, in metres, for Jason-2 cycle 6, over the European region covered by the ALADIN model.

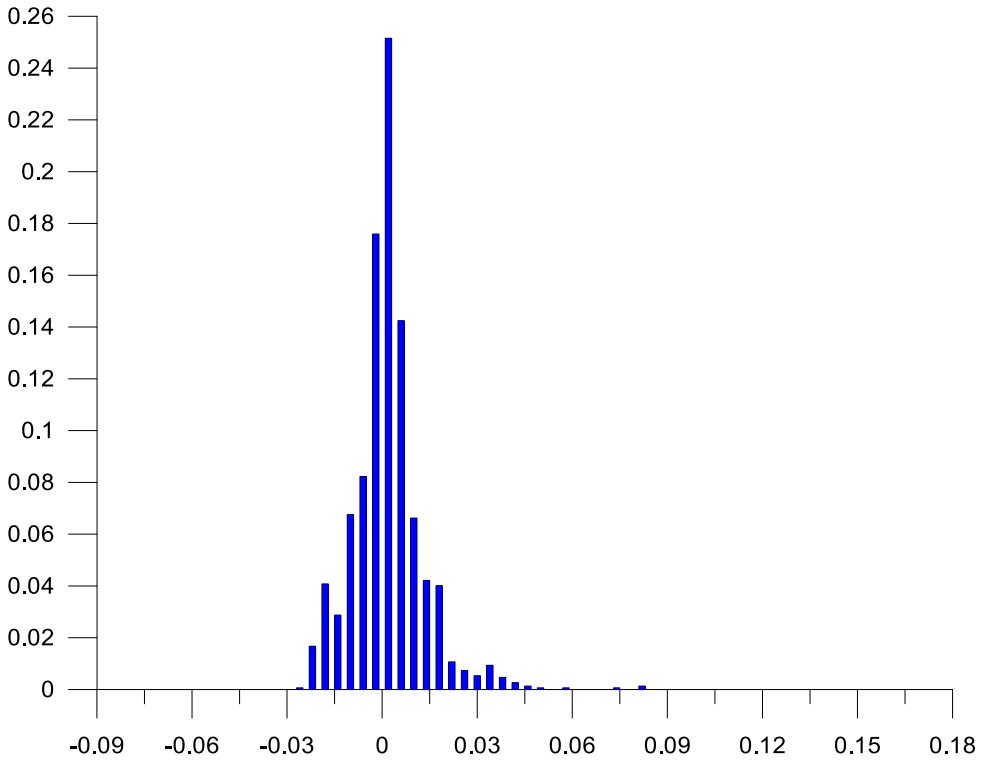

Fig.42 – Histogram of the differences between GPD and ECMWF corrections, in metres, for Jason-2 cycle 6, over the European region covered by the ALADIN model.

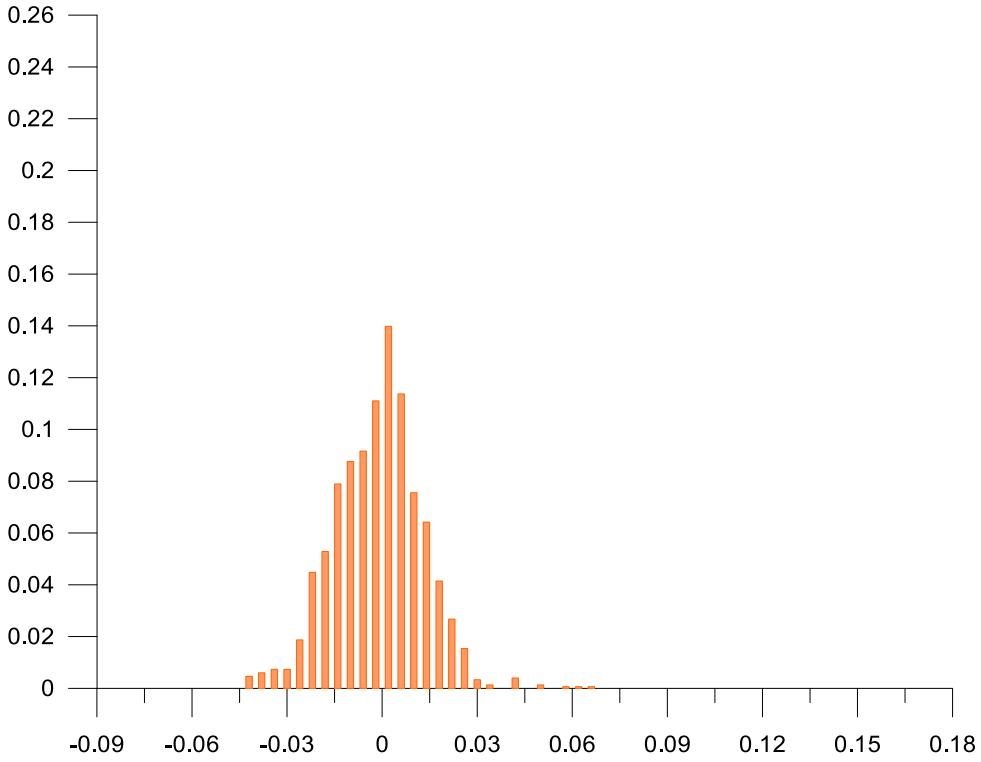

Fig.43 – Histogram of the differences between GPD and ALADIN corrections, in metres, for Jason-2 cycle 6, over the European region covered by the ALADIN model.

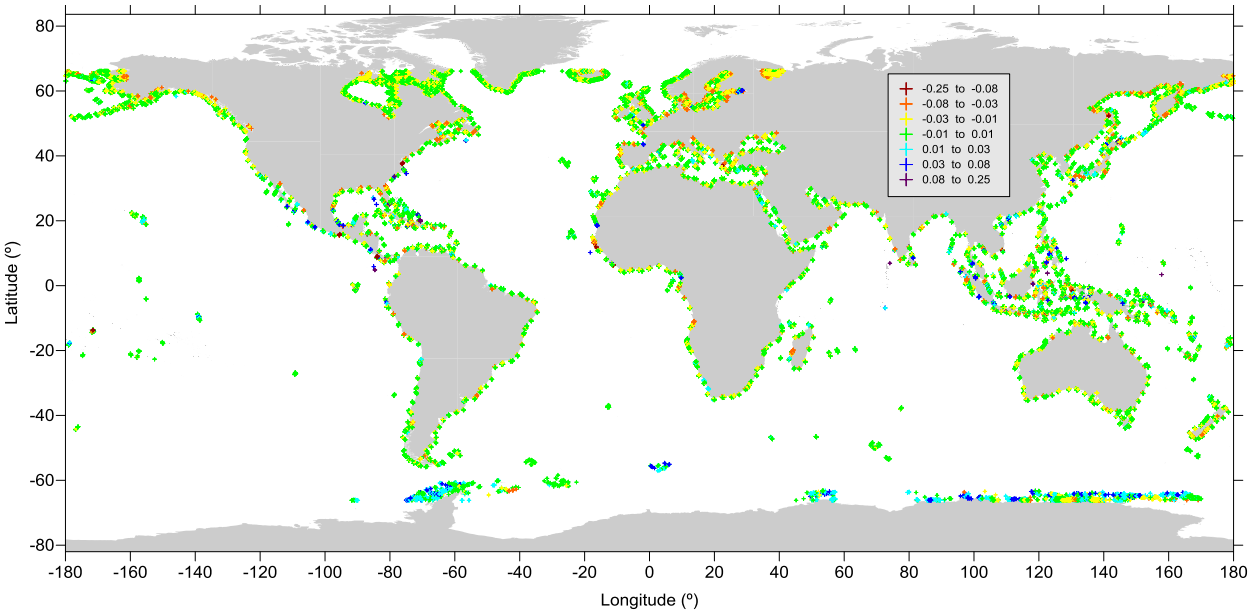

Fig.44 – Differences between GPD and MWR corr ---e ---ctions, in metres, for Jason-2 cycle 6.

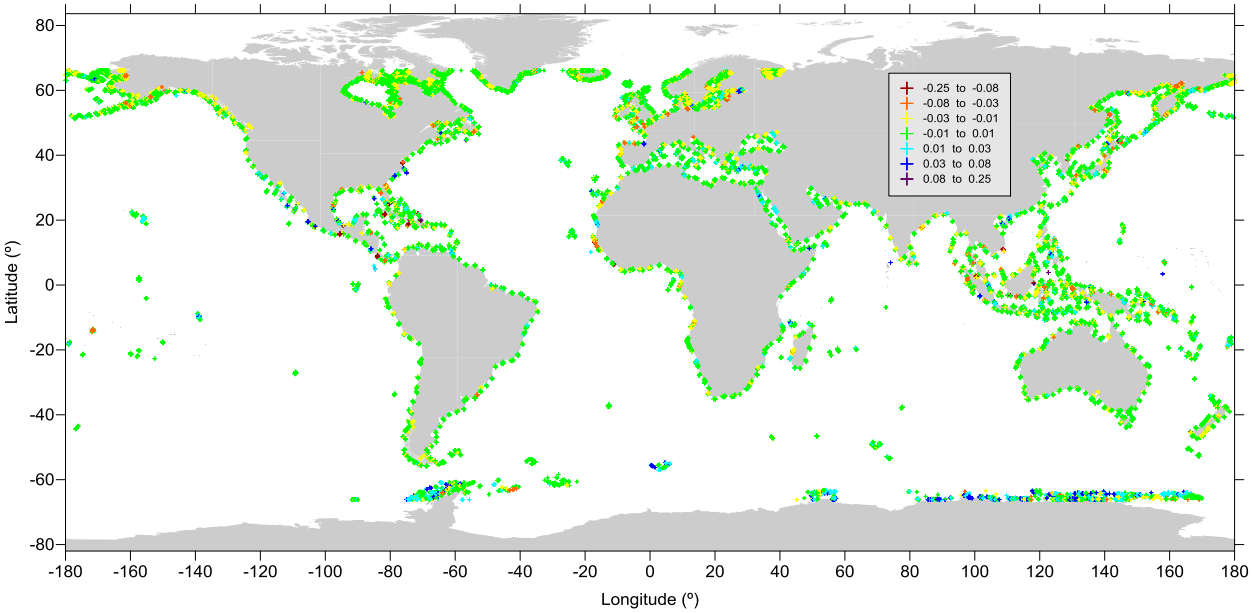

Fig.45 – Differences between GPD and MPA corrections, in metres, for Jason-2 cycle 6.

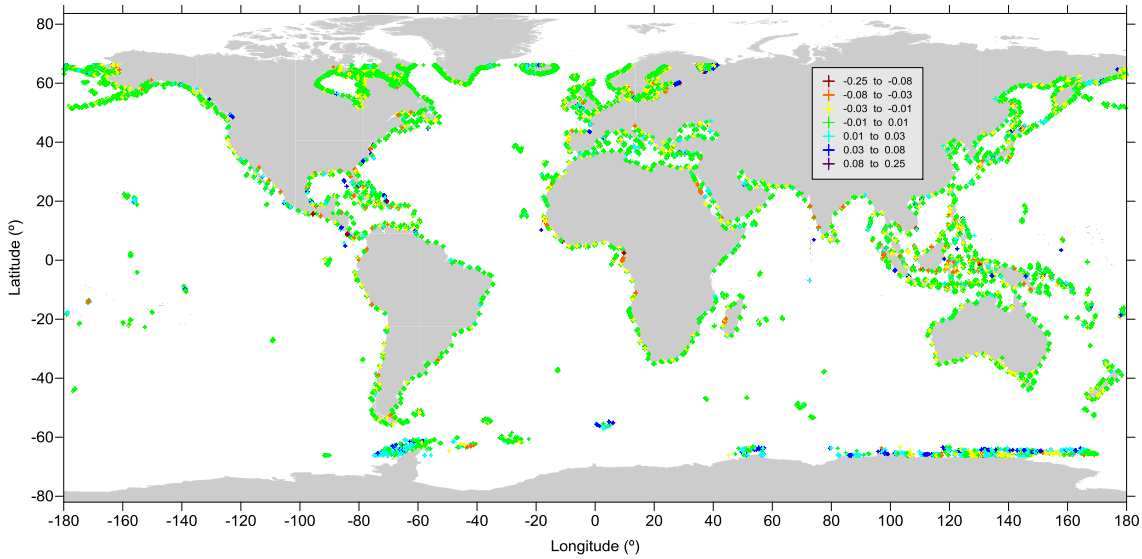

Fig.46 – Differences between GPD and LPA corrections, in metres, for Jason-2 cycle 6.

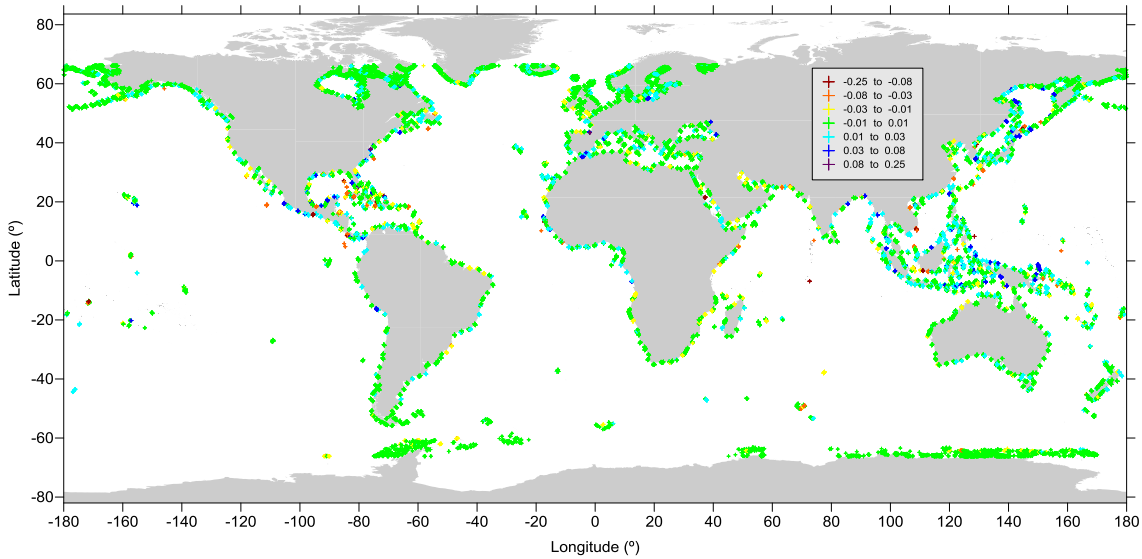

Fig.47 – Differences between GPD and ECMWF corrections, in metres, for Jason-2 cycle 6.

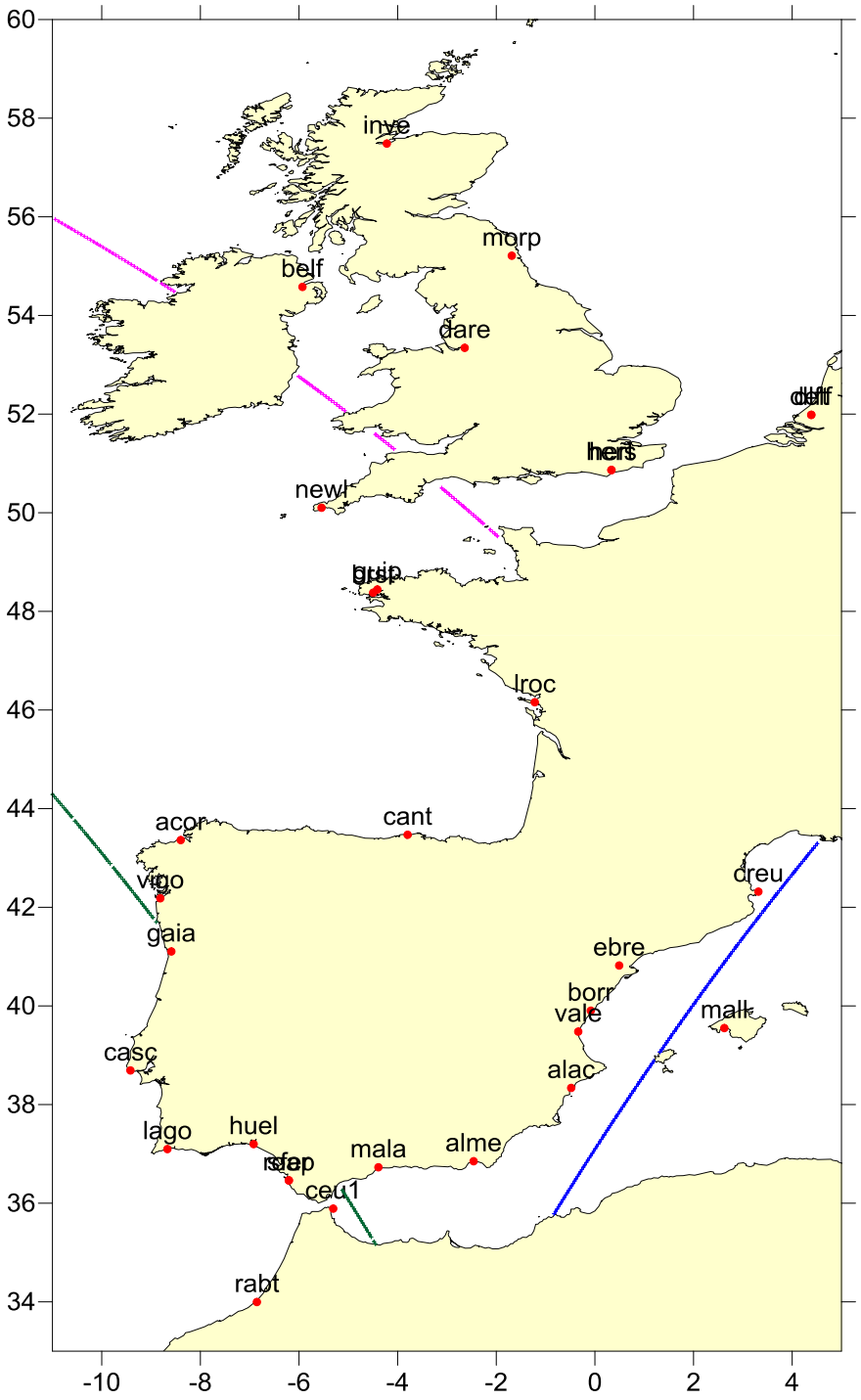

Fig.48 – Location of Jason-2 passes 20 (green), 146 (pink) and 187 (blue) analysed in this section.

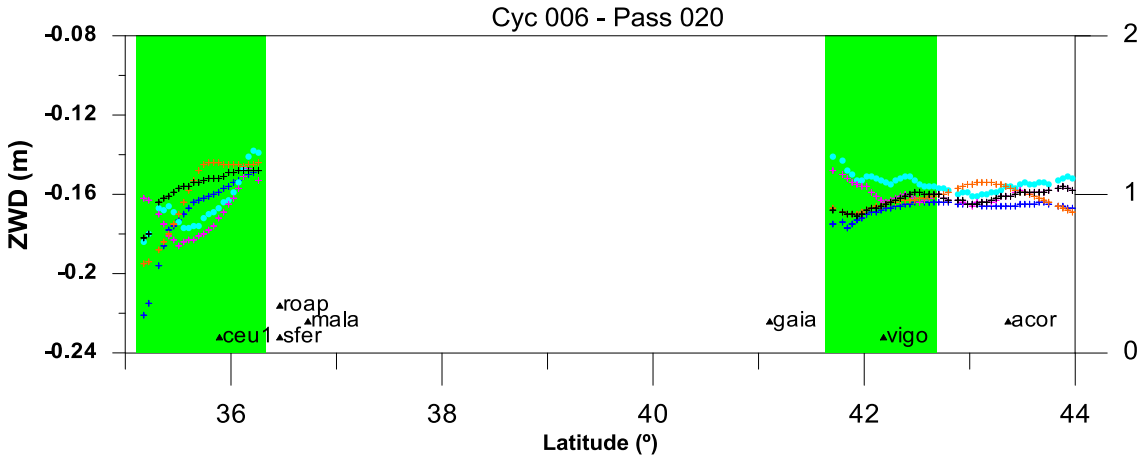

Fig.49 – ZWD for Jason-2 pass 20 cycle 6: ECMWF (blue), ALADIN (orange), GPD (black), MPA (cyan), LPA (pink) and original MWR wet tropospheric correction (red).

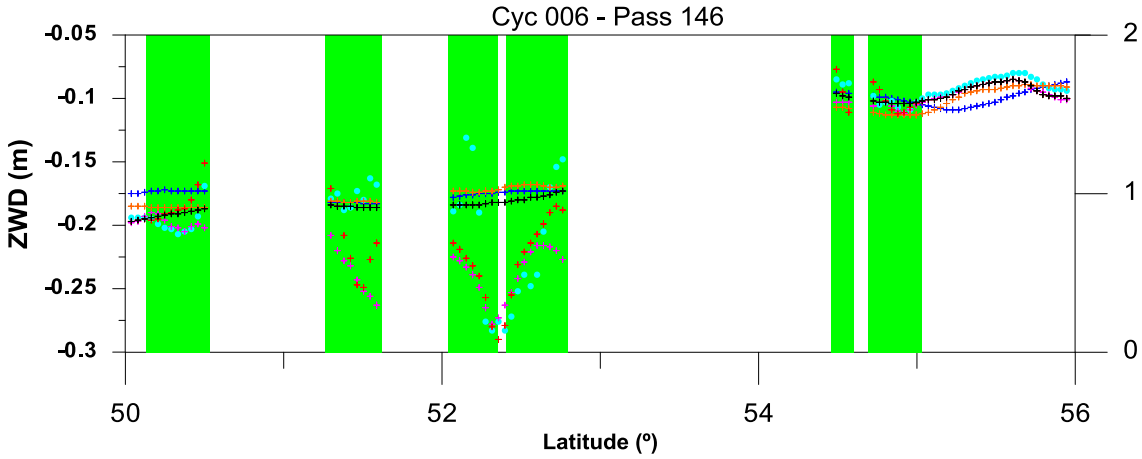

Fig.50 – ZWD for Jason-2 pass 146 cycle 6: ECMWF (blue), ALADIN (orange), GPD (black), MPA (cyan), LPA (pink) and original MWR wet tropospheric correction (red).

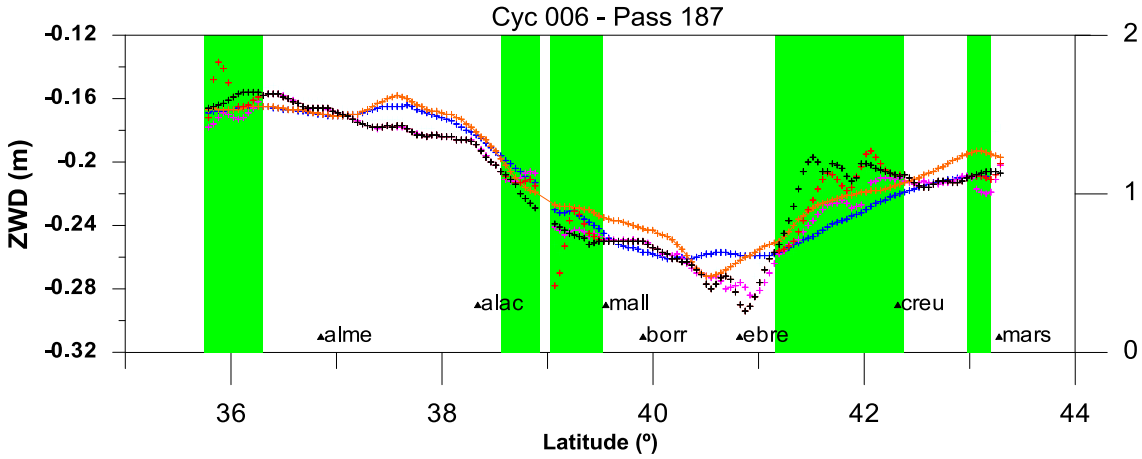

Fig.51 – ZWD for Jason-2 pass 187 cycle 6: ECMWF (blue), ALADIN (orange), GPD (black), MPA (cyan), LPA (pink) and original MWR wet tropospheric correction (red).

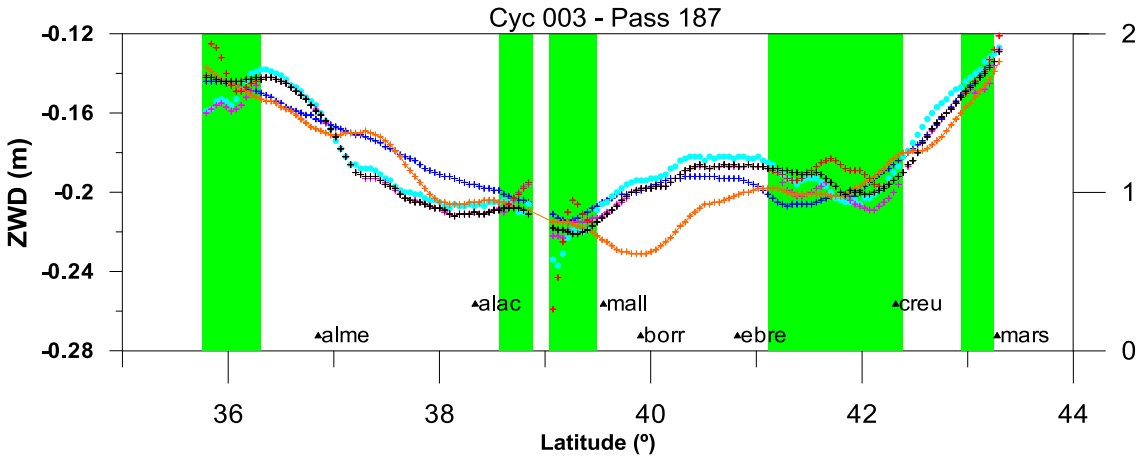

Fig.52 – ZWD for Jason-2 pass 187 cycle 3: ECMWF (blue), ALADIN (orange), GPD (black), MPA (cyan), LPA (pink) and original MWR wet tropospheric correction (red).

Figure 50 is an example of a region with small coastal tracks with only invalid MWR measurements, crossing the SW of Britain and Ireland. In these regions, the difficulty of MPA and LPA in retrieving a valid correction seems evident. In the absence of GNSS stations in these regions, the GPD estimate is solely based on ECMWF, which, at least in this example, also compares remarkably well with ALADIN. Although the derived correction might be too smooth, it seems more reliable than the MPA and LPA retrievals.

Overall, it is very difficult or impossible to say which of the tree algorithms is best. However, this analysis, which can be further extended to a larger period and other missions, allows identifying possible problems and improvements that might be applied to each algorithm. In addition, a better interpretation of the results would be possible with the participation of the authors of MPA and LPA algorithms.

3 Conclusions

Aiming to improve the data combination methodology used in the GPD algorithm, a study was conducted on the variability of the spatial correlation of the ZWD field using global ECMWF grids.

The analysis performed on the spatial correlations of the ZWD field, assuming isotropy, shows that the results are highly dependent on the size of the analysed domain. Considering the expected scales of interest the results obtained with cells of 2.5° degrees seem to be the most appropriate for adoption in the GPD algorithm. This analysis and the two-dimensional spatial analysis of the autocorrelation of the ZWD field clearly need to be pursued. We anticipate main difficulties related with basic, but very sensitive, steps that have to be taken prior to the computation of the autocorrelation of the ZWD field such as: the choice of the most suitable de-trending procedure to be adopted, if any, and the decision regarding the dimension of the spatial domain that encompasses the scales that better characterise the features of the atmospheric field being analysed. In addition, since the calculations over model grids may cause larger spatial correlation scales to be found, other data sets, such as MWR data, shall also be analysed.

Although the study performed on the full field assuming isotropy shows a clear dependence of the spatial correlation scale on latitude, this does not happen for the 2-D results on the de-trended field. This also needs further inspection to clarify if a latitudinal dependence of the correlation scale shall be implemented or not.

In the absence of ground truth a validation of the GPD wet tropospheric correction was performed by inter-comparisons with ECMWF and ALADIN models and with the other two available algorithms for the wet tropospheric correction in the coastal zone: MPA and LPA. Results for Jason-2 cycles 3, 4 and 6 are presented.

Knowing that *a priori* none of the mentioned fields can be considered as a reference field, this analysis, more than evaluating the accuracy of any of the ZWD estimates, allows the detection of possible problems in the various data sets and may point directions for improvements.

Results show that, overall, the three coastal PD algorithms show a common behaviour in most of the regions. However, there are tracks were the differences between the various corrections can reach several centimetres.

The standard deviation of the differences between all three coastal PD algorithms range from 10 to 15 mm, the closest retrievals being on average MPA and LPA. Although the differences are not statistically very significant, on average, GPD has differences with respect to the two models (ECMWF and ALADIN) smaller than MPA and LPA.

The comparison with ALADIN shows that this model reveals features that may depart significantly from the signals detected by the MWR in the open ocean.

Overall, it is very difficult or impossible to conclude if any of the three algorithms is better than the others everywhere. However, this analysis, which can be further extended to a larger period and other missions, allows identifying possible problems and improvements that might be applied to each algorithm.

Although in some regions the GPD estimates seem to produce more reliable corrections than the other two algorithms, which can show some noisy behaviour, we believe that a mixed approach, for example, a mixed MPA and GPD approach can improve the PD retrieval in some of the most problematic configurations.

Acknowledgements

The authors would like to acknowledge Météo-France for providing the ALADIN data and the European Centre for Medium Range Weather Forecasts (ECMWF) for providing the reanalysis data on the single-level atmospheric fields of the Deterministic Atmospheric Model datasets used within this study.

The authors would also like to acknowledge Radar Altimeter Database System (RADS) for providing the altimetric data and very gratefully thank Remko Scharroo (NOAA / Altimetrics LLC) for his prompt help and precious information about the data details for the various altimeters.

References

ALADIN (2009) http://www.cnrm.meteo.fr/aladin accessed on September 2009

Bennartz R. (1999) On the use of SSM/I measurements in coastal regions. J. Atmos. Oceanic Tech., vol. 16, pp. 417-431

Bosser, P., O. Bock, J. Pelon, C. Thom (2007) An improved mean-gravity model for GPS hydrostatic delay calibration. *IEEE Geosci. Remote Sens. Lett.*, vol. 4, no. 1, pp. 3–7

Bretherton, F.P., R.E. Davis, C.B. Fandry (2006) A technique for objective analysis and design of oceanographic experiment applied to MODE-73. Deep-Sea Res., vol. 23, pp. 559–582, 1976

Brown, S. (2010) A novel near-land radiometer wet path delay retrieval algorithm: application to the Jason-2/OSTM advanced microwave radiometer. IEEE Trans Geosci Remote Sens 48(4). doi:10.1109/TGRS.2009.2037220):

Desportes, C., E. Obligis and L. Eymard (2007) On the wet tropospheric correction for altimetry in coastal regions. IEEE Trans. Geosci. and Remote Sensing, vol 45, no 7, pp. 2139-2149

ECMWF (2009) http://www.ecmwf.int/products/catalogue/pseta.html

Fernandes M.J., C. Lázaro, A.L. Nunes, N. Pires, L. Bastos, V.B. Mendes (2010) GNSS-derived Path Delay: an approach to compute the wet tropospheric correction for coastal altimetry. Geosci Remote Sens Lett 7(3). doi:10.1109/LGRS.2010.2042425

Keihm, S., M.A. Janssen, C.S. Ruf (1995) TOPEX/Poseidon Microwave Radiometer (TMR): III. Wet troposphere range correction algorithm and pre-launch error budget. IEEE Trans. Geosci. Remote Sens., vol. 33, no. 1, pp. 147–161

Leeuwenburgh, O. (2000) Covariance modelling for merging of multisensory ocean surface data. In Methods and Applications of Inversion. New York: Springer-Verlag.

Obligis E., C. Desportes, L. Eymard, J. Fernandes, C. Lázaro, A. Nunes (2011) Tropospheric corrections for coastal altimetry. In: Vignudelli S, Kostianoy A, Cipollini P, Benveniste J (eds) Coastal Altimetry. Springer, Heidelberg, 560 pp. doi:10.1007/978-3-642-12796-0_6

Pannekoucke, O., L. Berre, G. Desroziers (2008) Background error correlation length-scale estimates and their sampling statistics. Q. J. R. Meteorol. Soc. 134: 497–511. doi: 10.1002/qj.212

Schüler T (2001) On Ground-Based GPS Tropospheric Delay Estimation. PhD Thesis, Universität der Bundeswehr München, Studiengang Geodäsie und Geoinformation available at http://ub.unibw-muenchen.de/dissertationen/ediss/schueler-torben/inhalt.pdf Accessed 13 January 2009